

Self-Supervised Training with Autoencoders for Visual Anomaly Detection

Alexander Bauer, Shinichi Nakajima, Klaus-Robert Müller

Abstract—Recently, deep autoencoders have been used for the task of anomaly detection in the visual domain. By optimizing for the reconstruction error using anomaly-free examples, the common belief is that a corresponding network should fail to accurately reconstruct anomalous regions in the application phase. This goal is typically addressed by controlling the capacity of the network, either by reducing the size of the bottleneck layer or by enforcing sparsity constraints on the activations. However, neither of these techniques does explicitly penalize reconstruction of anomalous signals often resulting in poor detection. We tackle this problem by adapting a self-supervised learning regime that allows the use of discriminative information during training but focuses on the data manifold of normal examples. Precisely, we investigate two different training objectives inspired by the task of neural image inpainting. Our main objective regularizes the model to produce locally consistent reconstructions, while replacing irregularities, therefore, acting as a filter that removes anomalous patterns. Our formal analysis shows that under mild conditions the corresponding model resembles a non-linear orthogonal projection of partially corrupted images onto the manifold of uncorrupted (defect-free) examples. This insight makes the reconstruction error a natural choice for defining the anomaly score of a sample according to its distance from a corresponding projection on the data manifold. We emphasize that inference with our approach is very efficient during training and prediction requiring a single forward pass for each input image. Our experiments on the MVTec AD dataset demonstrate high detection and localization performance. On the texture-subset, in particular, our approach consistently outperforms recent anomaly detection methods by a significant margin.

Index Terms—Anomaly detection, autoencoders, neural inpainting.



1 INTRODUCTION

THE task of anomaly detection in a broad sense corresponds to searching for patterns which considerably deviate from some concept of normality. Visual anomaly detection specifically aims to detect and locate anomalous regions in imagery data and has been used in many practical applications in the industrial [1]–[11], medical [12]–[15], and other domains [16], [17]. The criteria of what is normal and what is an anomaly can be very subtle and highly application dependent. The existing detection algorithms [1]–[11], [13], [18]–[60] typically assume the availability of normal examples only, while the anomalous examples are very scarce and are usually used to tune the hyperparameters of a corresponding model. The prevalent direction of research in the last two decades was focusing on the so-called one-class classifiers [18], [61] which aim at learning a tight decision boundary around the normal examples in a feature space and define a distance-based anomaly score relative to the center of the training data. The success of this approach strongly depends on the availability of suitable features. Therefore, it usually allows for detection of outliers

A. Bauer is with BASLEARN – TU Berlin/BASF Joint Lab for Machine Learning, Technische Universität Berlin, 10587 Berlin, Germany; alexander.bauer@tu-berlin.de.

S. Nakajima is with Berlin Institute for the Foundations of Learning and Data, Technische Universität Berlin, 10587 Berlin, Germany, and with RIKEN Center for AIP, Japan; nakajima@tu-berlin.de.

K.-R. Müller is with Berlin Institute for the Foundations of Learning and Data, Technische Universität Berlin, 10587 Berlin, Germany, and with Department of Artificial Intelligence, Korea University, Anam-dong, Seongbuk-gu, Seoul 02841, Korea, and with Max-Planck-Institut für Informatik, 66123 Saarbrücken, Germany; klaus-robot.mueller@tu-berlin.de.

(Corresponding authors: Alexander Bauer, Klaus-Robert Müller)

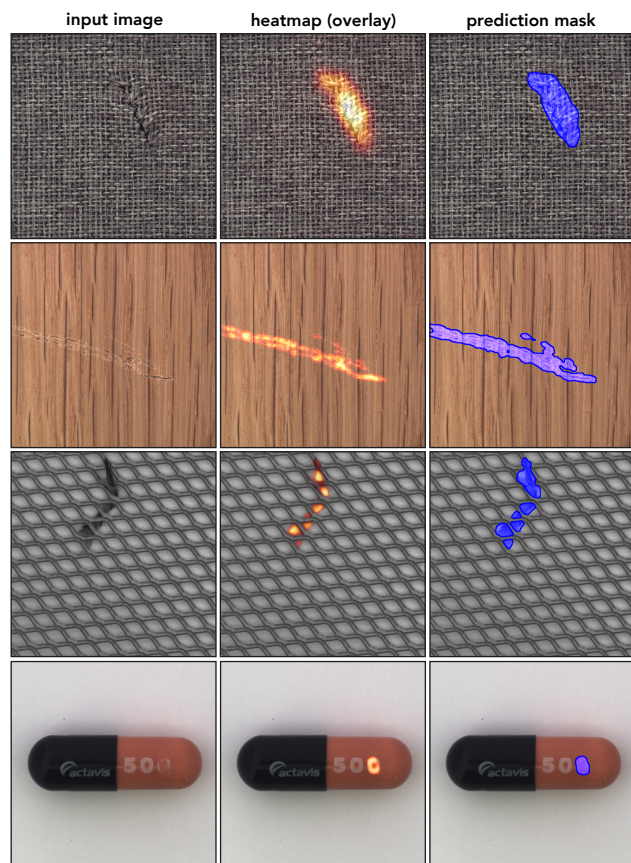


Fig. 1. Some anomaly detection results of our approach. Each row shows the input image, the overlay of a corresponding anomaly heatmap, and the resulting prediction mask, respectively.

only, which greatly deviate from the normal structure. In practice, however, we are often interested in more subtle deviations, which require a good representation of the data manifold. The same applies to the combined approach based on training deep neural networks (DNNs) directly with the one-class objective [19], [62], [63]. Although this objective encourages the network to concentrate the training data in a small region in the feature space, there is no explicit motivation for anomalous examples unseen during training to be mapped outside of the decision boundary. In other words, the one-class objective gives preference to models which map its input domain to a narrower region and does not explicitly focus on separating anomalous examples from the normal data.

Recently, deep autoencoders have been used for the task of anomaly detection in the visual domain [1], [49], [50]. Unlike one-class based approaches, they additionally allow for locating the anomalous regions in images by leveraging the pixel-wise nature of a corresponding training objective. By optimizing for the reconstruction error using anomaly-free examples, the common belief is that a corresponding network should fail to accurately reconstruct anomalous regions in the application phase. This goal is typically addressed by controlling the capacity of the network by either reducing the size of the bottleneck layer or enforcing some sparsity constraints on the inner activations [64], [65]. However, neither of these techniques does explicitly penalize reconstruction of anomalous signals often resulting in a poor detection. This is similar to the issue related to training with the one-class objective, where no explicit mechanism exists for preventing anomalous data points from being mapped to the normal region. In fact, an autoencoder optimized for the reconstruction error mainly aims to compress and accurately reconstruct the input images and does not care much about the actual distinction between normal and anomalous pixels. As a result, the reconstruction error for the anomalous and normal regions can be very similar preventing reliable detection and localization.

In this paper, we propose a self-supervised learning framework, which introduces discriminative information during training to prevent good reconstruction of anomalous patterns in the testing phase. We begin with an observation that the abnormality of a region in an image can be partially characterized according to how well it can be reconstructed from the context of the surrounding pixels. Imagine an image where a small patch has been cut out by setting the corresponding pixel values to zeros. We can try to reconstruct this patch by extrapolating the surrounding pixel values according to our knowledge about the patch distribution of the training data. If the reconstruction significantly deviates from the original image, we consider a corresponding patch to be anomalous and normal otherwise. Following this intuition, we feed partially distorted images to the network during training while forcing it to reconstruct the original content – similar to the task of neural image completion [66]–[70]. However, instead of setting the individual pixel values to zeros – as for the completion task – we apply a patch transformation, which approximately preserves the color distribution of the distorted regions, making it more difficult for the network to realize which image regions have been modified. In order to succeed,

the network now must learn features which are suitable for accomplishing two different tasks: a) detection of image regions deviating from an expected pattern and b) reconstruction of such regions from the neighboring pixel sets. Since this approach utilizes no explicit information (e.g., label mask) about the location of the anomalous regions – unlike for the task of semantic segmentation, for example – it regularizes the model to produce locally consistent reconstructions while replacing irregularities, therefore, acting as a filter that removes anomalous patterns.

Formally, the mapping implemented by a corresponding DNN approximates a non-linear orthogonal projection of partially corrupted images onto the data manifold consisting of anomaly-free examples. Given an orthogonal projection, we can naturally define the notion of anomalous examples according to their distance from the data manifold provided by the pixel-wise reconstruction error. The actual anomalous regions within the images can be identified from the pixel-wise contributions. We emphasize that our prediction process is very efficient as the entire image is processed in a single step - in contrast to related ideas based on sliding window approach [1], [50]. Figure 1 illustrates a few examples to give a sense of visual quality of the resulting segmentation masks when training according to our approach.

There is one potential issue with the above approach due to anomaly score being defined by the reconstruction error, which is sensitive to the variation of pixel intensities in the following sense. On the one hand, a high variation in pixel intensities (e. g. pepper noise) in the normal regions is likely to result in false positive detections. On the other hand, anomalous regions with a strong structural deviation might not be detected, if the color distribution of the corresponding pixels is of low contrast resulting in a small reconstruction error. To address this issue, we further experiment with our approach by modifying the training objective such that the network is penalized for producing a high reconstruction error in the normal regions while being rewarded for a higher reconstruction error in the distorted areas. The resulting network shows a kind of hybrid behavior. On the one hand it aims at reconstructing the normal regions and on the other hand it amplifies the reconstruction error for the anomalous regions by further disturbing the corresponding area, acting almost as a segmentation network. As we demonstrate in the experimental section, this modification might potentially improve the localization accuracy of the anomalous regions in comparison to our original idea based on filtering autoencoders.

The rest of the paper is organized as follows. In Section 2, we discuss the main differences of our approach to the related works. In Section 3, we formally introduce the proposed framework including training procedure, data generation process, and model architecture. Additionally, we provide a geometric interpretation of the resulting model by showing that it approximates a non-linear orthogonal projection of partially corrupted images onto the data manifold of uncorrupted examples. In Section 4, we evaluate the performance of our approach and provide the experimental results for the task of visual anomaly detection based on the publicly available MVTEC AD dataset [71], [72]. We finish our discussion with a conclusion in Section 5.

2 RELATED WORKS

In the context of automatic surface inspection, [1] proposed an anomaly detection approach based on neural image completion. Specifically, they train a convolutional neural network (CNN) to reconstruct small image patches for which a rectangular center area has been cut out. Using sliding window approach during prediction phase they compute a reconstruction error on the whole input image. To be able to complete the central region, a model must learn meaningful features, which allow to interpolate the local context. Although presenting an inspiring idea, this approach has two significant issues. First, cutting out an area prevents reconstruction of locally confined patterns, which cannot be computed from the context. Regardless if a corresponding pattern is anomalous or normal, it will be lost during the completion process resulting in a high reconstruction error. Second, the presented idea relies on a sliding window approach to detect anomalies at different image locations resulting in a slow inference during prediction phase. In contrast, we process the entire input image in a single step. Furthermore, our training objective does not rely on reconstruction of missing patches but rather aims at reproducing normal regions within the input image and either filtering anomalous patterns or enlarging the reconstruction difference for the areas which are inconsistent with their surrounding context. In particular, no information about the image is lost during the prediction phase allowing for an accurate reconstruction of the anomaly-free areas, which in turn improves the resulting performance for detection and localization of the anomalous regions.

The idea of using image inpainting for the task of anomaly detection has been pursued by multiple previous works. For example, (*LSR*) [3] aims at preventing reconstruction of anomalous patterns by projecting the input images to the normal regions in the latent space. The training and prediction phase are performed in two steps. Specifically, the authors first adopt a variational autoencoder as the reconstruction model to get a discrete latent space of normal samples. Then a deep autoregressive model is used to estimate the probability distribution of the training data in the latent space. In the detection stage this autoregressive model is used to determine which parts of the signal deviate from the data distribution in the latent space and should be resampled to yield a restored image, which is closest to the anomaly input. In contrast, our approach requires a single inference pass in both phases and requires no additional resampling.

More recent works (*CutPaste*, *InTra*, *RIAD*) [49], [50], [73] also rely on the idea of image inpainting originally introduced in [1]. The approach in [49], is similar to our idea in the sense that it also modifies input images to artificially create anomalous regions using a specific Cut&Paste augmentation technique. Unlike our method, however, it is a two-stage approach relying on training an additional binary classifier for detection and localization of the anomalous regions based on the visual explanation [74]–[76] algorithm called GradCAM [77]. The work in [73] replaces the sliding window procedure by a different approach. First the input image is divided in a grid of cells and a number of images is created by randomly removing some cells in the

original image. Inference is then performed on each single image and the resulting reconstruction is assembled from partial reconstructions of all images. The method in [50] further relies on the sliding window idea, but unlike other methods uses a self-attention based transformer instead of convolutional autoencoders. According to the authors, one drawback of their approach is the increased training time due to transformer architecture.

Another work (*DRAEM*) [51] closely related to our approach is based on similar idea to train a reconstruction model on partially corrupted images. However, we emphasize two main differences. First, the authors in [51] rely on a different procedure for generating artificial anomalous regions during training based on perlin-noise and out-of-distribution examples leveraging an additional data source. In contrast, we use gaussian distortion (or elastic deformation), which does not require additional data. Furthermore, it approximately preserves color distribution of the original patches making it more difficult for the model to realize which regions have been modified. This way the model can focus on difficult examples lying close to the manifold of normal data potentially resulting in more accurate predictions. Second, the approach in [51] uses an additional segmentation network on top of the reconstruction model for predicting the final mask for the anomalous regions. Both networks are trained jointly to provide accurate segmentation masks with less focus on the reconstruction accuracy due to a combined loss. In contrast, we rely more on the reconstruction ability of our model and propose a simple smoothing technique for computing the segmentation mask directly from the pixel-wise reconstruction map which requires no additional training and is computationally more efficient during the application phase. Since we do not train an additional model for mask segmentation, there is also no risk to overfit on the specific data used to generate anomalous regions. Finally, we motivate our approach by interpreting the resulting model as a filter for anomalous patterns, which resembles a non-linear orthogonal projection of corrupted examples onto the manifold of uncorrupted images. Altogether, these advantages lead to a higher performance on the MVTEC AD dataset [71], [72] - as we show in the experimental section.

Two recent works (*PatchCore*) [10] and (*PNI*) [52] report impressive results on the MVTEC AD dataset. Both are based on usage of memory banks comprising locally aware, nominal patch-level feature representations extracted from pre-trained networks. In contrast, our approach does not require additional storage place for the memory bank and performs on-par with the two methods. On the texture categories of the MVTEC AD dataset, in particular, our approach consistently outperforms the recent anomaly detection methods by a significant margin.

3 METHODOLOGY

We now introduce a self-supervised framework for training deep convolutional autoencoders to detect and localize anomalous regions in images. More precisely, we describe the objective function, the data generation process during training, and our choice of the model architecture. As a closing remark, we provide a geometric interpretation of

the resulting model as an approximation of a non-linear orthogonal projection of anomalous examples onto the data manifold populated by the anomaly-free images.

3.1 Training Objective

We use $F: [0, 1]^{n \times m \times 3} \rightarrow [0, 1]^{n \times m \times 3}$, $n, m \in \mathbb{N}$ to denote a mapping related to a DNN that implements an autoencoder with input and output tensors corresponding to color images. Furthermore, we denote by $X \in [0, 1]^{n \times m \times 3}$ an original image and by \hat{X} a copy of X , which has been partially modified. The modified regions within \hat{X} are marked by a binary¹ mask $M \in \{0, 1\}^{n \times m \times 3}$, where \bar{M} denotes a corresponding complement. Given this notation, our training objective can be written as follows:

$$\mathcal{L}(\hat{X}, X) = \frac{(1-\lambda)}{\|\bar{M}\|_1} \cdot \|\bar{M} \odot (F(\hat{X}) - X)\|_2 + \frac{\lambda}{\|M\|_1} \cdot \|M \odot (F(\hat{X}) - X)\|_2 \quad (1)$$

where \odot denotes an element-wise tensor multiplication and $\lambda \in [0, 1]$ is a weighting parameter for controlling the importance of the two terms during training. $\|\cdot\|_p$ for $p \in \mathbb{N}_+$ denotes the L^p -norm on a corresponding tensor space. In terms of supervised learning, we feed a partially modified image \hat{X} as input to the network, which we train to reconstruct the original image X representing the ground truth label. By minimizing the above objective, a corresponding autoencoder aims at learning to perform two tasks. The first term moves the network towards an accurate reconstruction of the masked input image $\bar{M} \odot X$ from a latent space, while the second term requires the network to correct corrupted regions $M \odot \hat{X}$ by restoring the original content. Altogether, the objective in equation (1) steers the behavior of a corresponding autoencoder to produce locally consistent reconstructions of the input images while replacing irregularities, acting, in some sense, as a filter for

1. For the sake of simplicity we first restrict the mask M and its complement \bar{M} to be binary. Later we will relax this assumption and consider real-valued tensors $M \in [0, 1]^{n \times m \times 3}$. A corresponding complement is then defined as $\bar{M} = 1 - M$ where 1 represents a tensor of the same size as M having value 1 at each index.

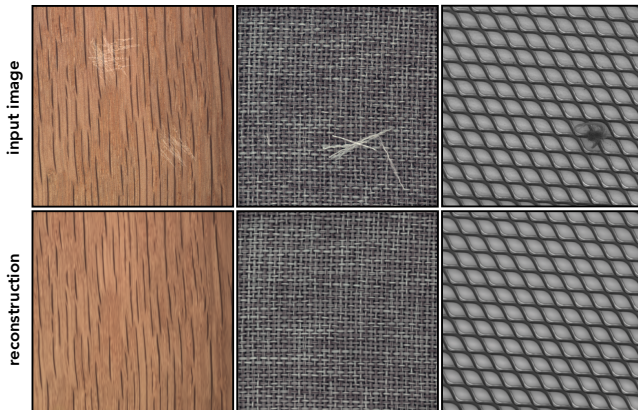


Fig. 2. Illustration of the reconstruction effect of a model trained either on the wood, carpet or grid images (without defects) from the MVTEC AD dataset using objective (1).

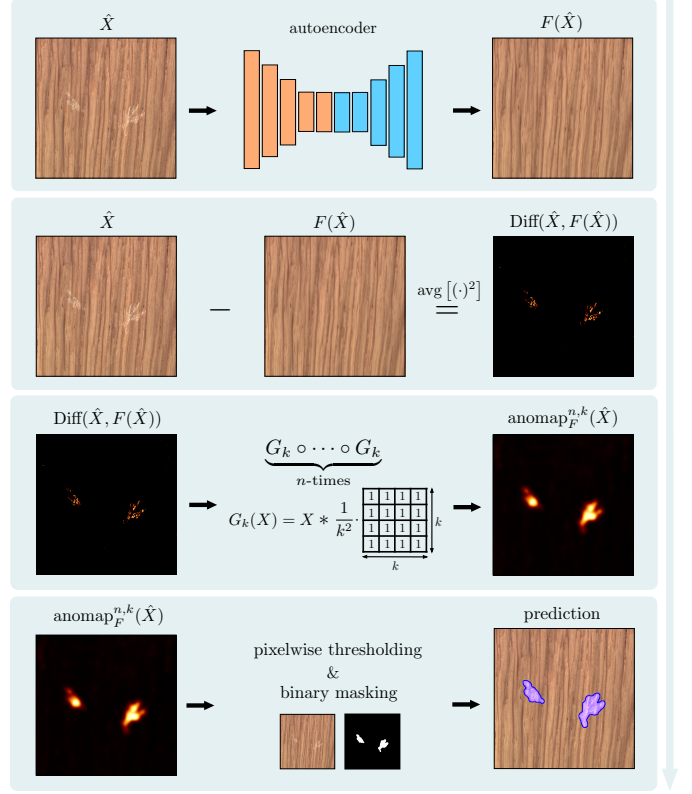


Fig. 3. Illustration of the anomaly detection process by our approach involving four different steps. In the first step an input image \hat{X} is passed to our model identified with the mapping F , which produces an output $F(\hat{X})$ by replicating normal regions and replacing irregularities with locally consistent patterns. In the second step we compute a pixel-wise squared difference $(\hat{X} - F(\hat{X}))^2$ between the input \hat{X} and the reconstruction $F(\hat{X})$, which is subsequently averaged over the color channels to produce the difference heatmap $\text{Diff}(\hat{X}, F(\hat{X}))$. In the third step we repeatedly (n -times) apply an averaging convolution G_k to the difference heatmap $\text{Diff}(\hat{X}, F(\hat{X}))$ producing our final anomaly heatmap $\text{anomap}_F^{n,k}(\hat{X})$. In the last step we compute a binary segmentation mask by thresholding the anomaly heatmap.

anomalous patterns. Figure 2 shows some reconstruction examples produced by our model trained with objective (1) either on wood, carpet or grid images (without defects) from the MVTEC AD dataset [71]. We can see how normal regions are accurately replicated by the model, while irregularities (e.g., scratches or threads) are replaced by locally consistent patterns.

Given a trained autoencoder F and an input image \hat{X} , we can perform anomaly detection by thresholding a corresponding difference heatmap $\text{Diff}(\hat{X}, F(\hat{X}))$ computed by averaging the (pixel-wise) squared difference $(\hat{X} - F(\hat{X}))^2$ over the color channels as follows

$$\text{Diff}(\hat{X}, F(\hat{X})) := \text{avg} \left[(\hat{X} - F(\hat{X}))^2 \right]. \quad (2)$$

To get a robust segmentation mask we smooth the difference heatmap before thresholding according to the following formula:

$$\text{anomap}_F^{n,k}(\hat{X}) := G_k^n(\text{Diff}(\hat{X}, F(\hat{X}))), \quad (3)$$

where $G_k^n = \underbrace{G_k \circ \dots \circ G_k}_{n\text{-times}}$ denotes a repeated application of a convolution mapping G_k defined by an averaging filter

of size $k \times k$ with all entries set to $1/k^2$. We treat the numbers $n, k \in \mathbb{N}$, $k \geq 1$ as hyperparameters, where G_k^0 is the identity mapping. We compute the anomaly score for the entire image \hat{X} from $\text{anomap}_F^{n,k}(\hat{X})$ by summing the scores for the individual pixels. For gray images with $n = 0$, this reduces to squared Frobenius norm $\|\hat{X} - F(\hat{X})\|_F^2$. The complete detection procedure is summarized in Figure 3.

In some cases, a model trained using objective (1) can fail to produce accurate detection results. As already mentioned in the introduction, a problem with the above approach is that the reconstruction error is sensitive to the pixel intensities. Anomalous regions even with a strong structural deviation from normal patterns but of low contrast might not be detected, if the reconstruction $F(\hat{X})$ has similar pixel intensities as the input \hat{X} (see Figure 11 for an example). One way to address this problem is to use a GMS-based smoothing scheme for the difference heatmap proposed in [50], [73]. Unfortunately, this can also amplify the background noise in the image increasing the number of false positive detections. Here, we investigate a different idea by adjusting our training objective in (1) to reward a higher reconstruction error in the distorted areas as follows:

$$\mathcal{L}(\hat{X}, X) = \frac{(1 - \lambda)}{\|\bar{M}\|_1} \cdot \|\bar{M} \odot (F(\hat{X}) - X)\|_2 - \frac{\lambda}{\|\bar{M}\|_1} \cdot \|\hat{X} - X\| \odot (F(\hat{X}) - X)\|_2 \quad (4)$$

Note the minus sign between the two terms in the above objective. The first term encourages the network to produce an accurate reconstruction of the normal regions, while the second term amplifies the reconstruction error for the modified area increasing the contrast in the resulting anomaly heatmap. Figure 4 illustrates some reconstruction results of a corresponding model when trained using the objective (4). Note how the anomalous regions are emphasized in the reconstruction image resembling, in some sense, the performance of a model trained for the task of semantic segmentation. In order to decrease the loss value, the network has to put more attention on the task of locating the anomalous regions potentially improving the final localization performance. For anomalous regions of low contrast this improvement can be dramatic as we show in the experimental section. Figure 11 provides some examples illustrating the qualitative difference between the two objectives in such a case.

There is one further detail in the objective (4) required to prevent the following unwanted effect. Depending on the type of transformation generating \hat{X} from X , the objective (4) can put too much weight on the second term. Namely, the loss can be easily decreased by setting the pixel values in $F(\hat{X})$ within the mask M to achieve maximal difference to the corresponding pixels in X completely ignoring the actual pixel difference $|\hat{X} - X|$. In particular, if some regions have exactly the same pixel values in both images, the objective (4) still encourages the network to increase the reconstruction error for these regions. We tackle this by replacing the mask M with a tensor $|\hat{X} - X| \in [0, 1]^{n \times m \times 3}$, therefore, adjusting the importance of the second term according to the relative pixel difference.

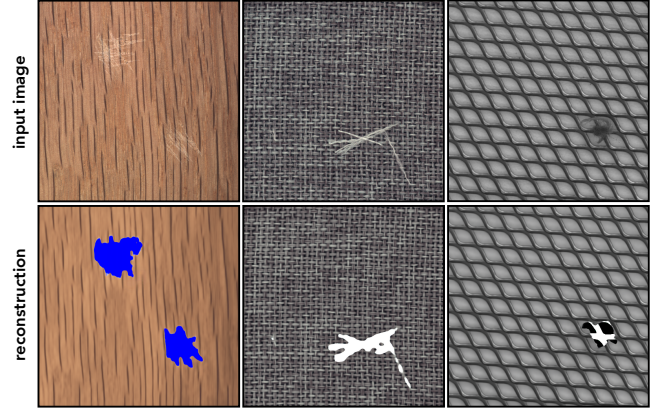


Fig. 4. Illustration of the reconstruction effect of a model trained either on the wood, carpet or grid images (without defects) from the MVTec AD dataset using objective (4).

3.2 Data Generation and Training

Since we use a self-supervised approach we need to provide a training data consisting of input-output pairs. The ground truth outputs are given by the original images corresponding to the normal examples. The inputs are generated from these images by partially modifying some regions as follows. For each image X , in the first step we randomly sample the size and the location of a patch to be modified. Then this patch is extracted and passed through an elastic deformation process corresponding to a gaussian distortion. Additionally, we randomly define a shape mask to smoothly glue the content of the modified patch with the original image. In the last step the shape mask is embedded in a two-dimensional zero-array at the location chosen in the first step to create a global mask represented by a real-valued tensor $M \in [0, 1]^{n \times m \times 3}$. Finally, a corresponding content of the original image X is replaced by the modified patch giving a corrupted image \hat{X} . The whole procedure is illustrated in Figure 5.

During training we sample normal images from the training data representing the outputs, from which we generate distorted inputs to be passed to the network. We experimented with different transformations of the original images like simple cut-out, patch swapping and elastic deformation with the latter providing the best results. We also found that it can be useful (depending on the data) to vary the brightness of modified patches. Furthermore, we use a progressive training scheme gradually increasing the size of the input images while keeping the same resolution over the course of the training phase. During testing phase there is no input modification and images are passed unchanged to the network. Anomalous regions are then detected by thresholding a corresponding anomaly heatmap computed from the difference between the inputs and the outputs of the model according to the formula in equation (3).

3.3 Model

We follow an established architecture of deep autoencoders, where the encoder is build from layers gradually decreasing spatial dimension and increasing the number of feature maps, while the decoder reverses this process by increasing

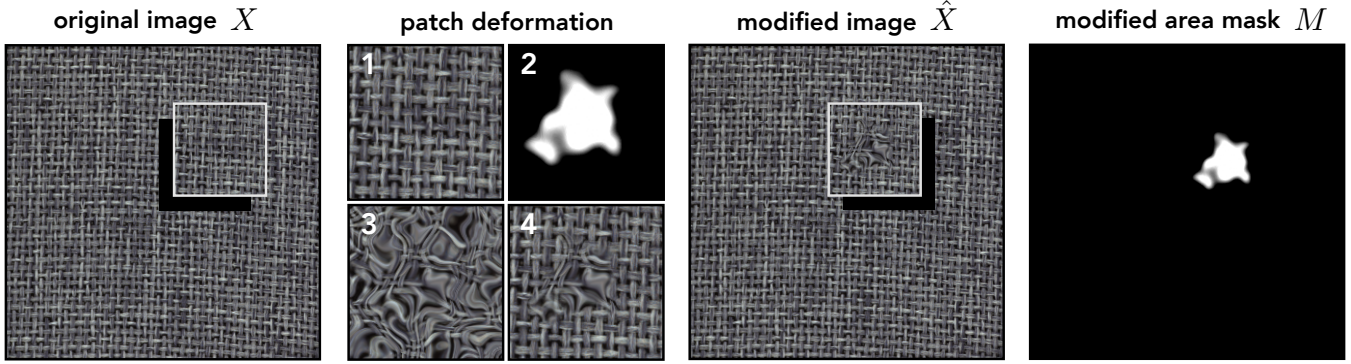


Fig. 5. Illustration of the process for generating artificial distortions within the training images. In the first step (see first image) we randomly choose the size and location of a patch to be modified. In the second step (see second image) a corresponding patch is extracted and transformed using elastic deformation by introducing gaussian distortions. Also a real-valued shape mask is created for the content of the transformed patch. The final modified patch to be placed in the original image is created according to the formula $X_4 = X_2 \odot X_3 + (\mathbf{1} - X_2) \odot X_1$ where X_1, X_2, X_3, X_4 represent the four patches in the second image and $\mathbf{1}$ is a tensor filled with one's. In the last step the shape mask X_2 is embedded in a 3-dimensional zero-array to create a global mask $M \in [0, 1]^{n \times m \times 3}$ and a corresponding content of the original image X is replaced by the modified patch X_4 giving the final image \hat{X} .

the spatial dimension and decreasing the number of channels. An important detail here is that additionally to the standard convolutions we exploit the dilated convolutions [78] for approximating higher order dependencies between the individual pixels and their local neighborhood. An overview of the whole architecture is given in Table 1. Here, after each convolution *Conv* (except in the last layer) we use batch normalization and rectified linear units (ReLU) as the activation function. Max-pooling *MaxPool* is applied to reduce the spatial dimension of the intermediate feature maps. *Transp. Conv* denotes the convolution transpose operation and also uses batch normalization with ReLUs. In the last layer we use a sigmoid activation function without batch normalization. We observed that using batch normal-

TABLE 1
Model architecture with a hyperparameter $f \in \{3, 5\}$.

Layer Type	Number of Filters	Filter Size	Output Size
Conv	64	3×3	$512 \times 512 \times 32$
Conv	64	3×3	$512 \times 512 \times 32$
MaxPool		$2 \times 2 / 2$	$256 \times 256 \times 32$
Conv	128	3×3	$256 \times 256 \times 64$
Conv	128	3×3	$256 \times 256 \times 64$
MaxPool		$2 \times 2 / 2$	$128 \times 128 \times 64$
Conv	256	3×3	$128 \times 128 \times 128$
Conv	256	3×3	$128 \times 128 \times 128$
MaxPool		$2 \times 2 / 2$	$64 \times 64 \times 128$
SDC _{1,2,4,8,16,32}	64×6	$f \times f$	$64 \times 64 \times 384$
SDC _{1,2,4,8,16,32}	64×6	$f \times f$	$64 \times 64 \times 384$
SDC _{1,2,4,8,16,32}	64×6	$f \times f$	$64 \times 64 \times 384$
SDC _{1,2,4,8,16,32}	64×6	$f \times f$	$64 \times 64 \times 384$
Transp. Conv	256	$3 \times 3 / 2$	$128 \times 128 \times 256$
Conv	256	3×3	$128 \times 128 \times 256$
Conv	256	3×3	$128 \times 128 \times 128$
Transp. Conv	128	$3 \times 3 / 2$	$256 \times 256 \times 128$
Conv	128	3×3	$256 \times 256 \times 128$
Conv	128	3×3	$256 \times 256 \times 64$
Transp. Conv	64	$3 \times 3 / 2$	$512 \times 512 \times 64$
Conv	64	3×3	$512 \times 512 \times 64$
Conv	64	3×3	$512 \times 512 \times 32$
Conv	3	1×1	$512 \times 512 \times 3$

ization in the last layer sometimes can lead to unwanted gridding effects in the reconstruction. SDC_{1,2,4,8,16,32} refers to a stacked dilated convolution where multiple dilated convolutions (with kernel width $f \in \{3, 5\}$) are stacked together. The corresponding subscript $\{1, 2, 4, 8, 16, 32\}$ denotes the dilation rates of the six individual convolutions in each stack. After each stack we add an additional convolutional layer with the kernel size 3×3 and the same number of feature maps as in the stack followed by a batch normalization and ReLU activation.

3.4 Geometric Interpretation

In the following, we present a geometric perspective on the mapping F resulting from training a reconstruction model according to the objective (1). For this purpose, we first introduce an auxiliary notation. For each formal statement we provide a proof in the supplements.

Without loss of generality, we consider gray-scale images and identify each image tensor $X \in \mathbb{R}^{n \times m}$ with a column vector $\mathbf{x} \in \mathbb{R}^N$, $N := n \cdot m$. Furthermore, we denote by $S \subset \{1, \dots, N\}$ and $\bar{S} := \{1, \dots, N\} \setminus S$ a set of pixel indices and its complement, respectively. We write $\mathbf{x}_S \in \mathbb{R}^{|S|}$ to denote a corresponding restriction of $\mathbf{x} \in \mathbb{R}^N$ to the indices in S . Regarding the task of anomaly detection, we denote by D a data manifold containing only normal images and by D_S a corresponding restriction of its elements \mathbf{x} to \mathbf{x}_S . For example, D could be a set of images of wooden surface without defects. Given D , we define a superset² $\hat{D} := \{\hat{\mathbf{x}} \in \mathbb{R}^N \mid \exists \mathbf{x} \in D, S \subseteq \{1, \dots, N\}: \hat{\mathbf{x}}_S = \mathbf{x}_S\} \supseteq D$. That is, each (corrupted) image $\hat{\mathbf{x}} \in \hat{D} \setminus D$ can be seen as being generated from a normal image $\mathbf{x} \in D$ by partial modification according to a set of pixel indices in S . When training with the objective (1), the corresponding model aims at learning a mapping F , that maps any (according to S) partially corrupted $\hat{\mathbf{x}} \in \hat{D}$, to an $\mathbf{x} \in D$, which agrees

2. Note that we can always choose $|S| = N$. In that case $\hat{D} = \mathbb{R}^N$. To keep the notation simple we omit additional requirement on $|S|$ in the definition of \hat{D} and assume implicitly that S is hyperconstrained according to some constant $|S| \leq k$ which we treat as a hyperparameter depending on the maximal size of the anomalous regions.

with \hat{x} on the subset \bar{S} . For the purpose of further analysis we capture this ideal case in an assumption below.

Assumption 1. The mapping $F: \hat{D} \rightarrow D$ resulting from training a model according to the objective (1) maps each $\hat{x} \in \hat{D}$ to $F(\hat{x}) = x \in D$ where $\hat{x}_{\bar{S}} = x_{\bar{S}}$ for some set of pixel indices $\bar{S} \subset \{1, \dots, N\}$ with maximal size $|\bar{S}|$.

Note that \hat{D} is implicitly defined by the choice of transformations we use to generate corrupted inputs. In other words, the form \hat{x}_S of the corresponding artificial distortions during training affects (as expected) the range of the anomalous patterns which can be detected in the application phase. For example, if we use a simple cut-out (i.e., setting pixels to zeros) modification, there is a high chance of overfitting on this specific pattern – as we show in the last column in Figure 11.

Based on the introduced notation, we now can formulate the following observation. Namely, the restriction $F|_{\hat{D}}$ resembles an orthogonal projection³ of locally corrupted examples $\hat{x} \in \hat{D}$ onto the data manifold D populated by the normal images (without defects). In general, $F|_{\mathbb{R}^N}$ is unlikely to be orthogonal. However, we can show that under reasonable assumptions, the restriction $F|_{\hat{D}}$ approximately behaves like an orthogonal mapping. More precisely, the likelihood for $F|_{\hat{D}}$ to be orthogonal is affected by the form of \hat{D} which can be characterized on the one hand by the size $|S|$ and on the other hand by the form \hat{x}_S of the corrupted regions used to generate \hat{D} from normal examples $x \in D$. We specify this dependency in the proposition below.

Proposition 1. Let $x, \hat{x} \in \mathbb{R}^N$ such that $\hat{x}_{\bar{S}} = x_{\bar{S}}$ for some $S \subset \{1, \dots, N\}$ and its complement $\bar{S} = \{1, \dots, N\} \setminus S$. For each $y \in \mathbb{R}^N$, the following holds true

$$\|x_S - y_S\| \leq \|x_{\bar{S}} - y_{\bar{S}}\| \implies \|\hat{x} - x\| \leq \|\hat{x} - y\|, \quad (5)$$

provided the corrupted region \hat{x}_S satisfies the condition

$$\|x_S - \tilde{x}_S\| \leq \max\{\|x_S - y_S\|, \|y_S - \tilde{x}_S\|\}, \quad (6)$$

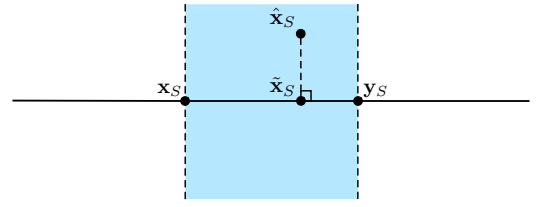
where \tilde{x}_S denotes the orthogonal projection of \hat{x}_S onto the line through x_S and y_S .

Note that the statement in the above proposition does not involve the mapping F and is a property of any finite-dimensional normed vector space (e.g., $(\mathbb{R}^N, \|\cdot\|_2)$). For a given $x \in D$, the condition in (6) restricts the form of the corrupted region \hat{x}_S , while the effect of its size $|S|$ is encoded through the implication in (5). There are two feasible (non-disjoint⁴) cases for \hat{x}_S represented by the condition in (6). Consider the line going through the points x_S and y_S . Each of the two cases is characterized by the proximity of \hat{x}_S to these two points which is uniquely determined by the distance from the orthogonal projection \tilde{x}_S (of \hat{x}_S) to x_S and y_S . See Figure 6 for an illustration. In the first case \tilde{x}_S lies on the line segment between x_S and y_S . In the second case x_S lies between \tilde{x}_S and y_S . In particular, the condition in (6) is fulfilled for all \hat{x}_S (see Case 1), which can be represented as a convex combination of x_S and y_S

3. For $\hat{D}, D \subseteq \mathbb{R}^n$ in a metric space (\mathbb{R}^n, d) , we call a (non-linear) mapping $F: \hat{D} \rightarrow D$ an **orthogonal projection** onto D if for each $\hat{x} \in \hat{D}$ the equality $d(\hat{x}, F(\hat{x})) = \inf_{x \in D} d(\hat{x}, x)$ holds.

4. The two cases share all elements which are projected to x_S .

Case 1: $\|x_S - y_S\| = \|x_S - \tilde{x}_S\| + \|\tilde{x}_S - y_S\|$



Case 2: $\|\tilde{x}_S - y_S\| = \|\tilde{x}_S - x_S\| + \|x_S - y_S\|$

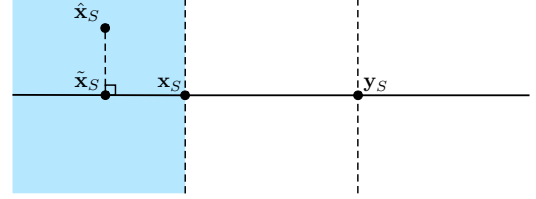


Fig. 6. Illustration of the condition (6) in Proposition 1 by distinguishing two feasible cases. Point \tilde{x}_S denotes the orthogonal projection of corrupted region \hat{x}_S on the line through the points x_S and y_S . The feasible area for \hat{x}_S in each case is marked with blue color.

including the important boundary case of patch swapping $\hat{x}_S = y_S$.

Informally, we would argue that the second case, which is more expressive with respect to the feasible form of corruption patterns \hat{x}_S , is also the most frequent one regarding the form of real anomalies. Consider for example the carpet images from the MVTEC AD dataset. It is not difficult to see that the test examples containing defects cannot be represented as a convex combination of normal images fulfilling the condition in (6) for many practical cases. Formally, by constraining $\hat{x}_S \in B_\epsilon(x_S)$ to lie within a closed ball around x_S with radius⁵ $\epsilon = \inf_{z_S \in D|_{\bar{S}} \setminus \{x_S\}} \|x_S - z_S\|$, we can ensure that the condition in (6) is fulfilled simultaneously for all $y \in D$.

By leveraging our Assumption 1 we can now link the results in Proposition 1 with the mapping F .

Theorem 1. Consider the mapping F in Assumption 1. For all $y \in D$ and $\hat{x} \in \hat{D}$ such that $F(\hat{x}) = x \in D$ with $\hat{x}_{\bar{S}} = x_{\bar{S}}$ for some $\bar{S} \subset \{1, \dots, N\}$, the following is true

$$\|x_S - y_S\| \leq \|x_{\bar{S}} - y_{\bar{S}}\| \implies \|\hat{x} - F(\hat{x})\| \leq \|\hat{x} - y\|, \quad (7)$$

provided the corrupted region \hat{x}_S satisfies the condition

$$\|x_S - \tilde{x}_S\| \leq \max\{\|x_S - y_S\|, \|y_S - \tilde{x}_S\|\}, \quad (8)$$

where \tilde{x}_S denotes the orthogonal projection of \hat{x}_S onto the line through x_S and y_S .

Given two data points $\hat{x} \in \hat{D}$ and $y \in D$, Theorem 1 specifies the conditions under which the inequality $\|\hat{x} - F(\hat{x})\| \leq \|\hat{x} - y\|$ holds. While the condition in (8) specifies the form of feasible corruptions \hat{x}_S , the premise of the implication in (7) is affected by the size of corrupted regions $|S|$ and is a property of the dataset of normal examples D .

5. For practical cases of a finite dataset D , we get a radius $\epsilon > 0$.

In the following, we turn our attention to the premise in (7) to investigate when the corresponding inequality holds depending on the quantities $|S|$ and $|\bar{S}|$. In order to simplify our analysis of the likelihood of this premise to be true, we restrict ourselves to images where all pixels are identically distributed, that is, $P(x_i) = P(x_j)$ for all $i, j \in \{1, \dots, N\}$. Note that this restriction allows for complex patterns and includes all examples corresponding to the texture categories in the MVTEC AD dataset. We support this claim by empirical evaluation in Figure 8 in Section 4. Based on the assumption of identical pixel distribution, we can state the following proposition.

Proposition 2. Consider a joint probability distribution P over pairs of images (\mathbf{x}, \mathbf{y}) with $P(\mathbf{x}, \mathbf{y}) = P(\mathbf{x}) \cdot P(\mathbf{y})$ and $P(x_i) = P(x_j) = P(y_k)$ for all $\mathbf{x}, \mathbf{y} \in D$, $\mathbf{x} \neq \mathbf{y}$ and $i, j, k \in \{1, \dots, N\}$. Then for all $S \subset \{1, \dots, N\}$, $\bar{S} = \{1, \dots, N\} \setminus S$ the following equality holds:

$$\mathbf{E}_{(\mathbf{x}, \mathbf{y})} [\|\mathbf{x}_S - \mathbf{y}_S\|^2 - \|\mathbf{x}_{\bar{S}} - \mathbf{y}_{\bar{S}}\|^2] = (|S| - |\bar{S}|) \cdot 2\sigma, \quad (9)$$

where $\mathbf{E}[\cdot]$, $\mathbf{Var}[\cdot]$ are the expectation and variance operators with respect to P and $\sigma = \mathbf{Var}[x_i]$ for some $i \in \{1, \dots, N\}$.

It follows directly (due to $\sigma > 0$) from equation (9) that $|S| \leq |\bar{S}|$ is a necessary condition in order for our premise $\|\mathbf{x}_S - \mathbf{y}_S\| \leq \|\mathbf{x}_{\bar{S}} - \mathbf{y}_{\bar{S}}\|$ in (7) to be true⁶. Furthermore, the expected value in (9) correlates with the number of pairs $(\mathbf{x}, \mathbf{y}) \in D \times D$, which violate the assumption $\|\mathbf{x}_S - \mathbf{y}_S\| \leq \|\mathbf{x}_{\bar{S}} - \mathbf{y}_{\bar{S}}\|$. Therefore, we can decrease their number according to (9) by decreasing $|S|$ corresponding to the size of corrupted regions.

The following theorem describes more specifically how the ratio $|S|/|\bar{S}|$ affects the number of pairs (\mathbf{x}, \mathbf{y}) potentially violating the premise in (7). Additionally to the identical marginal distribution of pixels, we now assume that a corresponding joint distribution is a Markov random field (MRF) [79]–[84]. That is, the conditional probability of a pixel depends only on a close neighborhood surrounding that pixel. See Figure 7 for an illustration. Furthermore, we define the notion of a distance $|i - j|_G$ between two nodes x_i and x_j in a graph G (identified with an MRF), which corresponds to the number of edges on a shortest path connecting the two nodes.

Theorem 2. Let $(\{x_1, \dots, x_N\})_{N \in \mathbb{N}}$, $(\{y_1, \dots, y_N\})_{N \in \mathbb{N}}$ be a pair of sequences of MRFs over identically distributed variables x_i, y_j with finite variance $\mathbf{Var}[x_i] = \sigma < \infty$ and vanishing covariance

$$\mathbf{Cov}[x_i, x_j] \rightarrow 0 \text{ for } |i - j|_G \rightarrow \infty. \quad (10)$$

Then for all $S \subseteq \{1, \dots, N\}$, $\bar{S} = \{1, \dots, N\} \setminus S$ with a fixed ratio $|S|/|\bar{S}|$, $|\bar{S}| > 0$ such that

$$|S| \leq 2 \cdot \sigma \cdot |\bar{S}|, \quad (11)$$

the following holds true:

$$\lim_{N \rightarrow \infty} P(\|\mathbf{x}_S - \mathbf{y}_S\| > \|\mathbf{x}_{\bar{S}} - \mathbf{y}_{\bar{S}}\|) = 0. \quad (12)$$

That is, given a reasonably⁷ large dimension $N \in \mathbb{N}$ of our

6. Note: $\|\mathbf{x}_S - \mathbf{y}_S\| \leq \|\mathbf{x}_{\bar{S}} - \mathbf{y}_{\bar{S}}\| \iff \|\mathbf{x}_S - \mathbf{y}_S\|^2 - \|\mathbf{x}_{\bar{S}} - \mathbf{y}_{\bar{S}}\|^2 \leq 0$.

7. We performed an empirical evaluation on images of size 512×512 (that is, with $N = 512^2$) from the texture categories of the MVTEC dataset with a satisfying result. Precisely, there were zero number of violating pairs when varying S and \bar{S} according to $|S| \leq 2 \cdot \sigma \cdot |\bar{S}|$.

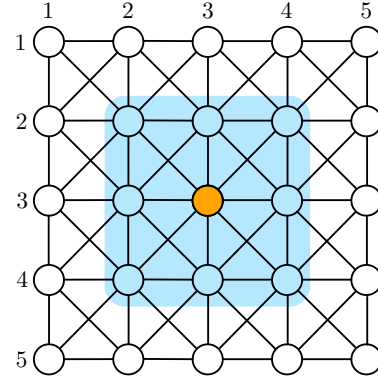


Fig. 7. Illustration of an MRF with 5×5 . The blue area marks the local neighborhood (of order 1) of the node $x_{3,3}$ (emphasized with orange color). Since we are dealing with image tensors, we can assume that the variables representing pixels are organized in a 2-dimensional grid of an MRF. Given a graph with nodes x_1, \dots, x_N , the Markov property assumes conditional independence according to $P(x_i | x_1, \dots, \hat{x}_i, \dots, x_N) = P(x_i | N(x_i))$, where $N(x_i) \subset \{x_1, \dots, \hat{x}_i, \dots, x_N\}$ is a local neighborhood around the node x_i containing all variables which can be reached from x_i by a number of edges upper bounded by the order of Markov property. The notation $(x_1, \dots, \hat{x}_i, \dots, x_N)$ implies that x_i is omitted.

image vectors in $D \subset [0, 1]^N$, we can ensure (in probability) that the number of pairs $(\mathbf{x}, \mathbf{y}) \in D \times D$, which violate the condition $\|\mathbf{x}_S - \mathbf{y}_S\| \leq \|\mathbf{x}_{\bar{S}} - \mathbf{y}_{\bar{S}}\|$, is zero by restricting the size of corrupted regions S according to $|S| \leq 2 \cdot \sigma \cdot |\bar{S}|$. We provide a deeper discussion regarding the assumption in (10) in the supplements.

To summarize, we showed that under specific conditions relating the form and size of corrupted regions, our mapping $F|_D$ resembles an orthogonal projection onto the manifold of normal examples. In the experimental section, we evaluate (see Figure 9) how well F approximates an orthogonal mapping in relation to $|S|$ on a real example. Given the orthogonality of F , we can naturally measure the degree of abnormality of an image $\hat{\mathbf{x}}$ according to the distance $\|\hat{\mathbf{x}} - F(\hat{\mathbf{x}})\|$ between $\hat{\mathbf{x}}$ and its orthogonal projection $F(\hat{\mathbf{x}})$ onto the data manifold of defect-free examples. This provides a geometric motivation for our definition of anomaly score as the shortest distance between an anomalous sample and the points on the data manifold.

4 EXPERIMENTAL ANALYSIS

In this section we evaluate the performance of our approach for the task of visual anomaly detection and compare the results with the existing methods.

4.1 Data and Setup

We used the public MVTEC Anomaly Detection dataset [71], [72] in our experiments consisting of 5 texture and 10 object categories. The texture categories cover both regular (carpet, grid) and random (leather, tile, wood) pattern cases. This dataset has been widely used as a benchmark for anomaly detection and localization in the manufacturing domain. To increase the amount of the training data in our experiments, we used simple data augmentation like rotation by a multiple of 90 degrees, as well as horizontal and vertical flipping depending on the category. We used 5% of the training data as validation set.

For each category we trained a separate model according to the architecture in Table 1 by minimizing either the objective (1) or (4). For the texture categories we used the same image resolution of 512×512 pixels and the kernel width $f = 3$ for the stacked dilated convolution layers. For the object categories we varied the input resolution in the range $\{256, 384, 512\}$ and the kernel width $f \in \{3, 5\}$. To train the weights of the model we used AdamOptimizer [85] with initial learning rate of 10^{-4} . For the object categories we used a slightly different procedure for smoothing the difference heatmap than presented in Section 3.1. Precisely, we compute an average heatmap

$$\text{avgmap}_F^{n,k}(V) := \frac{1}{|V|} \sum_{X \in V} \text{anomap}_F^{n,k}(X) \quad (13)$$

from the validation data V and modify our final anomaly heatmap according to

$$\overline{\text{anomap}}_F^{n,k}(\hat{X}) := \text{anomap}_F^{n,k}(\hat{X}) \odot (1 - \text{avgmap}_F^{n,k}(V))^t, \quad (14)$$

where $k, n, t \in \mathbb{N}$, $k \geq 1$ are hyperparameters.

For some cases (including the categories carpet, tile, bottle, cable, capsule, metal nut, transistor, zipper) we were able to slightly improve the final performance by using an alternative way for computing the difference heatmap $\text{Diff}(\hat{X}, F(\hat{X}))$ in equation (2). Precisely, instead of computing the pixel-wise squared difference $(\hat{X} - F(\hat{X}))^2$, we used the so-called similarity index SSIM [86] as a distance measure before the smoothing step in equation (3).

To evaluate the detection and localization performance of our model, we report the (image-wise and pixel-wise) area under the ROC (AUROC) metric, which is independent of the chosen threshold for the anomaly score.

4.2 Validation of Theoretical Claims

First we provide in Figure 8 empirical evidence supporting our assumption in Proposition 2 concerning the marginal probability distribution over the pixel values for texture categories. More precisely, we estimate the empirical mean and the standard deviation of the pixel values as follows. We resize the images in our training data to 512×512 pixels and compute the corresponding statistics from all sliding windows of the size 256×256 . For the texture categories we show the empirical mean and the standard deviation for each pixel. For the sake of presentation, we visualize the corresponding statistics for object categories only for pixels which lie on the horizontal line through the middle of the images. In particular, the plots for the texture categories support our assumption of identical distribution for pixel values. That is, $P(x_i) = P(x_j)$ for each pair of pixels i, j .

Next we present in Figure 9 some measurements regarding the orthogonality of our model F trained (on the carpet category) with objective (1). For this purpose we conducted the following experiment. In the first step, for each image X in our training data D of defect-free examples we repeatedly generated a new image \hat{X} by randomly choosing the position of a squared patch of width $\sqrt{|S|}$ and replacing it by another patch from a different (randomly chosen) image. In the second step, we evaluated the terms $\text{argmin}_{Y \in D} \|\hat{X} - Y\|$ and $\text{argmin}_{Y \in D} \|F(\hat{X}) - Y\|$ while

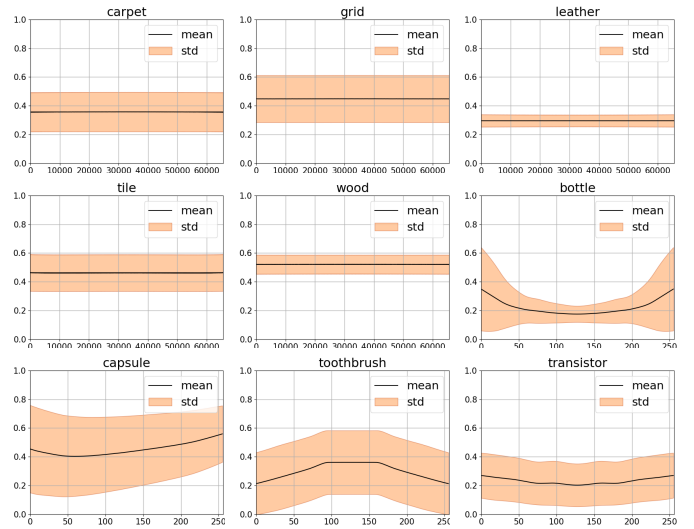


Fig. 8. Illustration of the first two moments of the marginal pixel distribution $P(x_i)$ for some categories in the MVTec AD dataset. In each plot the x-axis marks the position of a pixel within a flattened image and y-axis shows the estimated mean and standard deviation for the values of that pixel. For the texture categories (carpet, grid, leather, tile, wood) we plot the values for each pixel in a 256×256 image, while for the object categories (bottle, capsule, toothbrush, transistor) we consider only the pixels lying on the horizontal line through the middle of the image. In particular, the plots for the texture categories support our claim that the condition $P(x_i) = P(x_j)$ holds true for all pixels i, j .

varying the size $|S|$ of the corrupted (replaced) patches. During the experiment we counted the frequency of X being the minimizer of the above terms. Intuitively, in order for F to be approximately orthogonal, we need to get X in the most cases. The corresponding accuracy as a function of the normalized width (given as $\sqrt{|S|/N}$) of the replaced patch is shown in the first two plots in Figure 9. The red dotted line marks the patch width corresponding to $|S|/N = 0.5$ where the corrupted region constitutes 50% of the original image. As we can see, for a reasonable choice of $|S|/N < 0.5$, the corrupted images \hat{X} and the outputs $F(\hat{X})$ lie closer to the target image X among all $Y \in D$. The third plot in Figure 9 additionally illustrates how close the outputs $F(\hat{X})$ are to the actual target X . Similarly to the first experiment, we repeatedly generated artificial images \hat{X} from X while varying the size $|S|$ of corrupted patches. However, instead of counting the minimizing arguments, we measure the distances $\|F(\hat{X}) - X\|$ and compute the corresponding mean and standard deviation. Again we can see that for a reasonable choice of $|S|$ the reconstruction quality is very high. In particular, our measurements show $\|F(X) - X\|/N \approx 0$ for $X \in D$. See Figure 2 for some reconstruction examples.

4.3 Results

To evaluate the segmentation accuracy of our model trained with objective (1), we report the pixel-wise AUROC metric and compare our results to the recent state-of-the-art algorithms in Table 2. Additionally, we report the AUROC metric on the image-level to estimate the detection performance and compare the results with the top-ranking methods in Table 3. Our method achieves high detection and localization

TABLE 2
Experimental results for the anomaly segmentation task given as **AUROC** on the pixel-level for each category in the MVTec AD dataset.

Category	AnoGAN [6]	CNNFD [7]	VAE [9]	AE _{SSIM} [2]	FCDD [48]	LSR [3]	RIAD [73]	CutPaste [49]	InTra [50]	DRAEM [51]	PatchCore [10]	PNI [52]	Ours
carpet	54	72	78	87	96	94	96.3	98.3	99.2	95.5	98.7	99.4	99.7
grid	58	59	73	94	91	99	98.8	97.5	98.8	99.7	98.8	99.2	99.7
leather	64	87	95	78	98	99	99.8	99.5	98.6	99.6	99.3	99.6	99.7
tile	50	93	80	59	91	88	89.1	90.5	94.4	99.2	96.3	98.4	99.2
wood	62	91	77	73	88	87	85.8	95.5	88.7	96.4	95.2	97.0	98.1
avg. textures	57.6	80.4	80.6	78.2	92.8	93.4	93.9	96.3	96.1	97.9	97.7	98.7	99.3
bottle	86	78	87	93	97	95	98.4	97.6	97.1	99.1	98.6	98.9	98.6
cable	86	78	87	82	90	95	94.2	90.0	91.0	94.7	98.7	99.1	98.2
capsule	84	84	74	94	93	93	92.8	97.4	97.7	94.3	99.1	99.3	99.1
hazelnut	87	72	98	97	95	95	96.1	97.3	98.3	99.7	98.8	99.4	98.9
metal nut	76	82	94	89	94	91	92.5	93.1	93.3	99.5	99.0	99.3	98.5
pill	87	68	83	91	81	95	95.7	95.7	98.3	97.6	98.6	99.0	99.3
screw	80	87	97	96	86	96	98.8	96.7	99.5	97.6	99.5	99.6	99.7
toothbrush	90	77	94	92	94	97	98.9	98.1	98.9	98.1	98.9	99.1	99.1
transistor	80	66	93	90	88	91	87.7	96.1	96.1	90.9	97.1	98.0	98.6
zipper	78	76	78	88	92	98	97.8	99.3	99.2	98.8	99.0	99.4	99.5
avg. objects	83.4	76.8	88.5	91.2	91.0	94.6	95.3	95.8	96.9	97.0	98.7	99.1	99.0
avg. all	74.8	78.0	85.9	86.7	91.6	94.2	94.8	96.0	96.7	97.3	98.4	99.0	99.1

TABLE 3
Experimental results for the anomaly detection task given as **AUROC** on the image-level for each category in the MVTec AD dataset.

Category	AnoGAN [6]	CNNFD [7]	VAE [9]	AE _{SSIM} [2]	FCDD [48]	LSR [3]	RIAD [73]	CutPaste [49]	InTra [50]	DRAEM [51]	PatchCore [10]	PNI [52]	Ours
carpet	49	63	78	67	99	71	84.2	93.1	98.8	97.0	98.2	100	100
grid	51	67	73	69	95	91	99.6	99.9	100	99.9	98.3	98.4	100
leather	52	67	95	46	99	96	100	100	100	100	100	100	100
tile	51	71	80	52	98	95	93.4	93.4	98.2	99.6	98.9	100	100
wood	68	84	77	83	94	96	93.0	98.6	97.5	99.1	99.9	99.6	100
avg. textures	54.2	70.4	80.6	63.4	97.0	89.8	94.0	97.0	98.9	99.1	99.0	99.6	100
bottle	69	53	87	88	96	99	99.9	98.3	100	99.2	100	100	100
cable	53	61	90	61	93	72	81.9	80.6	70.3	91.8	99.7	99.8	98.0
capsule	58	41	74	61	95	68	88.4	96.2	86.5	98.5	98.1	99.7	98.2
hazelnut	50	49	98	54	97	94	83.3	97.3	95.7	100	100	100	100
metal nut	50	65	94	54	98	83	88.5	99.3	96.9	98.7	100	100	100
pill	62	46	83	60	97	68	83.8	92.4	90.2	98.9	97.1	96.9	99.5
screw	35	43	97	51	93	80	84.5	86.3	95.7	93.9	99.0	99.5	98.9
toothbrush	57	57	94	74	95	92	100	98.3	100	100	98.9	99.7	100
transistor	67	58	93	52	90	73	90.9	95.5	93.1	99.7	99.7	100	98.8
zipper	59	54	78	80	98	97	98.1	99.4	99.4	100	99.7	99.9	100
avg. objects	56.0	52.7	88.8	63.5	95.2	82.6	89.9	94.4	93.1	97.4	99.2	99.5	99.3
avg. all	55.4	54.6	86.1	63.5	95.8	85.0	91.3	95.2	95.0	98.0	99.2	99.6	99.6

performance on the challenging MVTec AD dataset. On the texture categories, in particular, it consistently outperforms recent state-of-the-art algorithms by some margin. Interestingly, the same holds for texture-like object categories including pill, toothbrush and zipper. At the beginning, our approach suffered the most on object categories like cable, screw and transistor for the following reasons. Many of the defects for the cable category like cable swapping, for example, are not covered by the elastic deformation technique that we use to generate artificial distortions during training. In order to improve the test performance, we apply additionally to the elastic deformation (in an alternating manner) one further modification resulting in partial occlusion of the input image by several shapes with content from a different data source similarly to the training idea in [51]. The screw category on the other hand contains a great amount of irrelevant background in the image preventing the model from focusing on the object itself. For such cases we could increase the detection performance by extracting (and aligning) the objects of interest from the image. Instead, we additionally used the same occlusion technique as for the cable category in our experiments. The same applies to the transistor category, for which we further augmented the data distortion process by randomly rotating the corrupted images around the center. This seems to be an important detail in order to achieve high detection and segmentation results on the examples from the test data, where the object

of interest is either shifted or is completely missing.

Our empirical evaluation suggests that training a reconstruction model according to the objective (1), on average, provides more accurate results than the alternative approach with objective (4). For comparison, we report the corresponding metrics on image and pixel-level in Table 4 for the texture categories in the MVTec AD dataset. Although being less accurate on average, we observed that objective (4) can sometimes provide highly accurate segmentation results. We conjecture that the resulting segmentation accuracy, when training with objective (4), is affected by the choice of the specific transformations, which are used during training to create corrupted inputs. By adopting the corresponding

TABLE 4
Experimental comparison of two proposed training objectives given as **AUROC** on the pixel-level and image-level for each texture category in the MVTec AD dataset.

Category	image-level		pixel-level		Ens.
	Obj. (1)	Obj. (4)	Obj. (1)	Obj. (4)	
carpet	100	100	99.7	99.7	99.7
grid	100	99.5	99.7	98.9	99.7
leather	100	97.9	99.6	98.6	99.6
tile	100	100	99.2	98.7	99.2
wood	100	99.0	98.1	97.1	98.3
avg. all	100	99.3	99.3	98.6	99.3

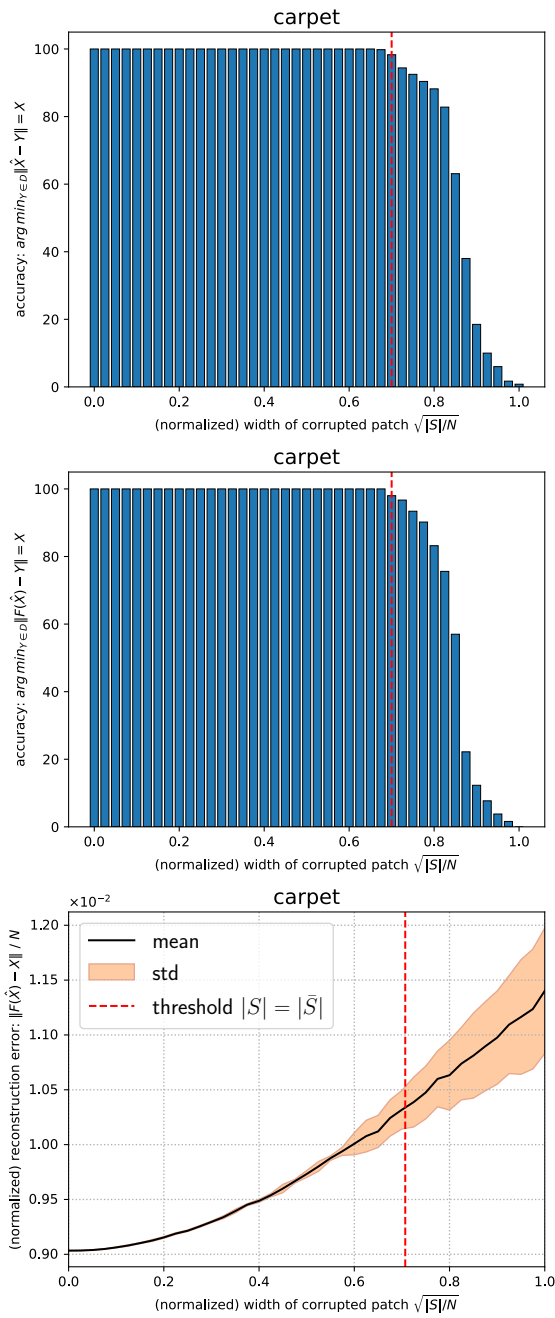


Fig. 9. Illustration of the orthogonality measurement for a trained model F as a function of the normalized width $\sqrt{|S|/N}$ of corrupted patches on the example of carpet category from MVTEC AD data. The upper two plots show that for a reasonable size of the corrupted area $|S|/N < 0.5$, the mapping F satisfies the property $\|\hat{X} - F(\hat{X})\| = \inf_{Y \in D} \|\hat{X} - Y\|$. The dotted red line marks the threshold corresponding to $|S| = |\bar{S}|$. The lower plot shows the variation in the reconstruction error $\|F(\hat{X}) - X\|$.

transformation process according to the expected type of anomalous pattern, a model trained with objective (4) can potentially achieve a higher detection and localization performance. To support this claim, we visualize in Figure 11 the difference in quality of the anomaly heatmaps for the two objectives on a few examples of liquid contamination on the wooden surface. The corresponding columns in the figure show the input image, the ground truth label mask,

the anomaly heatmap according to objective (4) using Elastic Deformation for image modification, the anomaly heatmap according to objective (1) using Elastic Deformation for image modification, and the anomaly heatmap according to objective (1) using the replacement-by-zeros as the image modification technique, respectively. Based on this insight, we additionally provide the results (see last column in Table 4) of a simple ensemble method combining the models trained separately with objective (1) and (4) as follows. In the first step we compute the anomaly heatmaps anomap_1 and anomap_2 for the two models. In the second step we combine the two heatmaps by taking the pixel-wise maximum: $\text{anomap}_{\text{Ens}} = \max\{\text{anomap}_1, \text{anomap}_2\}$. This simple idea increased the segmentation result for the wood category by 0.2 points suggesting a potential for further improvement through a combination of the two approaches.

To summarize, the experimental results show that our model trained according to the objective (1) provides (on average) more accurate results for both detection and localization of the anomalous regions than the objective (4). Furthermore, it consistently outperforms the previous methods on the texture categories from the MVTEC AD dataset. To give a sense of visual quality of the resulting segmentation masks when training with objective (1), we show a few examples in Figure 1 and further examples in Figure 10.

4.4 Discussion

We presented two different objectives (1) and (4) for training an autoencoder for the task of detecting and segmenting anomalous regions in images. For practical cases we can use either of the two to get an accurate model. In the following, we discuss some important differences of the two approaches.

The objective (1) is a more robust and practical choice to work with. There is a good measure of training progress given by the reconstruction error, which strongly correlates with the ability of the model to remove anomalous patterns from images. Therefore, reconstruction error provides a good choice for our target loss. Also the search for the weighting parameter λ is rather straightforward – setting $\lambda = 0.5$ turns out to be sufficiently good in many cases. Furthermore, elastic deformation as a distortion technique seems to provide enough discriminative information during training to detect various kinds of anomalous patterns on the texture categories from the MVTEC AD dataset. However, as previously mentioned, we used additional modifications like occlusion and rotation of the images to improve the performance on some object categories. We found that a combination of these modification techniques provides better results than their use in isolation. Interestingly, a corresponding model tends to act as a filter for anomalous patterns by replacing irregularities with locally consistent reconstructions. Therefore, it can also detect more subtle anomalous patterns lying close to the data manifold of normal examples.

The objective (4) produces a model, which behaves more similar to a segmentation network. Therefore, it can potentially provide more accurate segmentation results. For the same reason, however, the objective (4) is more sensitive to the choice of modification method that we use during training to create corrupted examples. Therefore, it is more prone

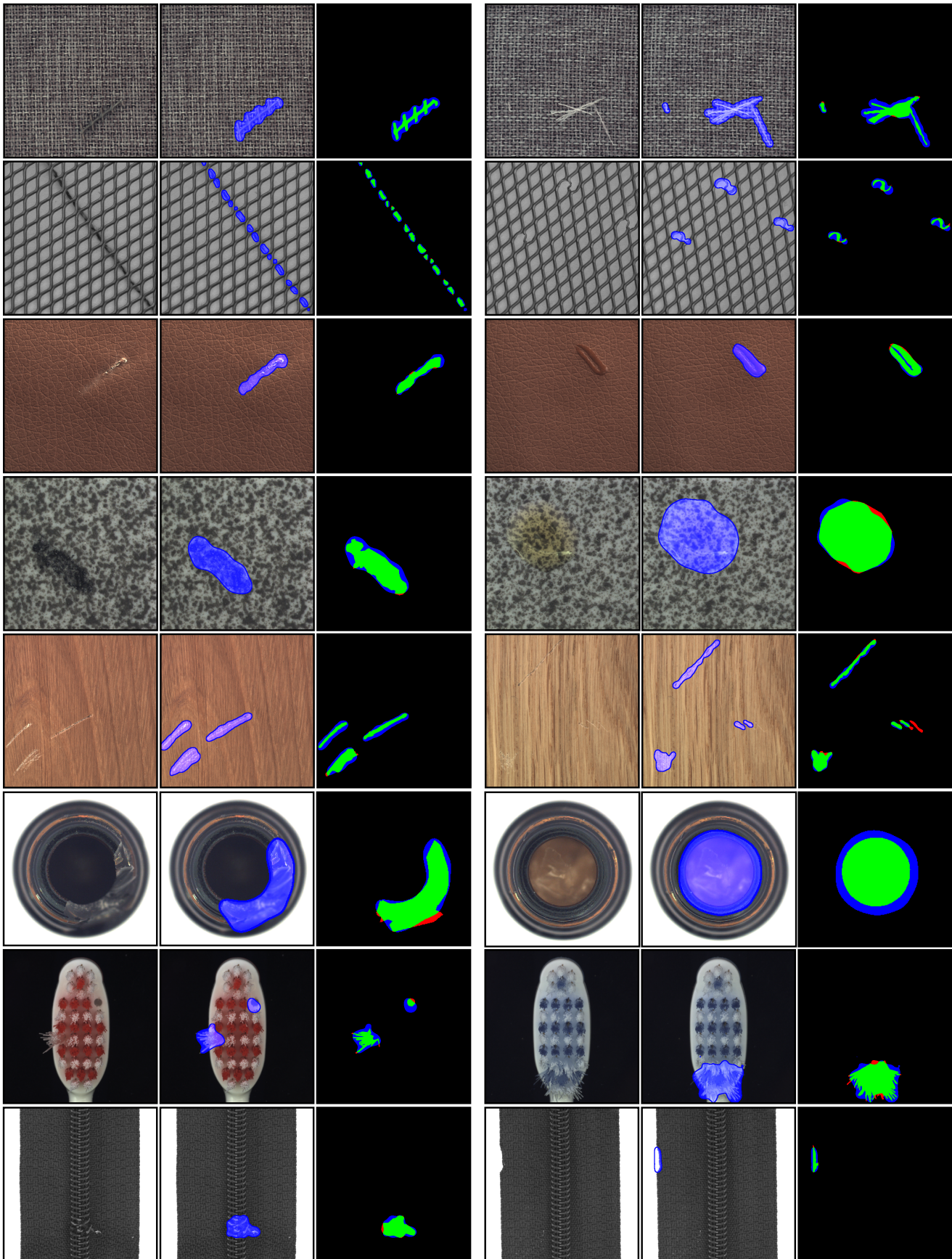


Fig. 10. Illustration of anomaly segmentation results when training according to the objective (1). Each row shows two random examples from the texture and some object categories in the MVTEC AD dataset. The columns show the input image, the prediction mask for the anomalous regions and the evaluation map with respect to the ground truth masks provided with the dataset. The colors green, blue and red in the evaluation map encode the true positives, false positives and false negatives, respectively.

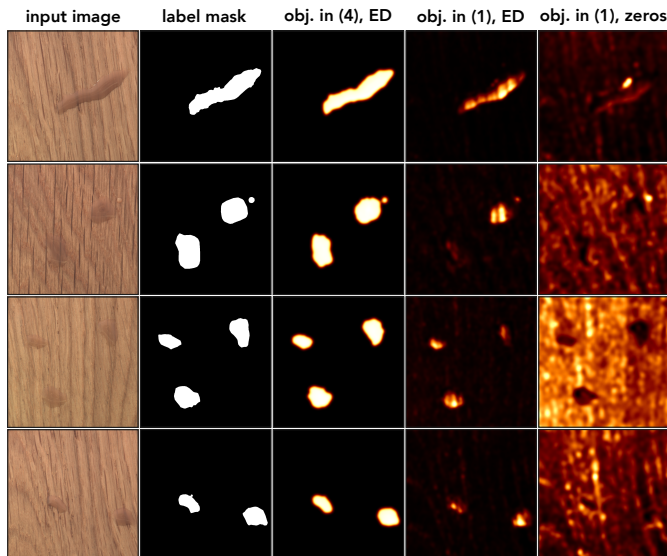


Fig. 11. Illustration of the qualitative performance difference when training either with objective (4) (third column) or (1) (fourth and fifth column) on a few examples of glue drops on the wooden surface. The first two columns show the input images and the ground truth label masks provided with the MVTec AD dataset. "ED" indicates that Elastic Deformation has been used for creating modified patches during training. "zeros" indicates that modified area has been cut out by setting the corresponding pixel values to zeros.

to overfitting and we must rely on early stopping to get accurate results. Also the search for good λ values is more difficult because the second term in the objective (4) tends to influence the training in a less predictable way. Despite all the difficulties, the increase in the localization performance can be very significant in comparison to objective (1) as we showed in Figure 11 for the case of glue drops on a wooden surface. We plan on investigating how the specific form of image modifications affects the overfitting during training in the future works. It is worth mentioning that training a model in a supervised way by using a segmentation loss directly on the artificially generated anomalies does not provide good results. It begins to overfit on the specific type of chosen artificial patterns already after a few training epochs. More specifically, it quickly learns to locate the elastic deformation patterns but completely fails to detect real anomalies from the test set.

As a final remark we note that the results in Table 4 suggest a potential improvement by creating an ensemble from models trained separately via objective (1) and (4).

5 CONCLUSION

We presented a self-supervised learning framework for the task of visual anomaly detection. Precisely, we train a deep convolutional autoencoder on partially distorted images to reconstruct the inputs with one of the two proposed objectives. Our approach benefits from using discriminative information during training which allows it to better distinguish between normal and anomalous regions in the testing phase. However, unlike pure discriminative approaches (e.g., semantic segmentation), our method focuses on the data manifold of normal examples resulting in a more

robust detection and localization performance with respect to anomalies in the images.

A model trained via objective (1) acts as a filter for anomalous patterns by replacing irregularities with locally consistent reconstructions. Due to this fact, it is capable of detecting a variety of anomalous patterns - even those which lie very close to the data manifold populated by the normal examples. In particular, we showed that the resulting model resembles an orthogonal projection onto this manifold supporting our choice for defining the anomaly score by means of the reconstruction error, that is, as a shortest distance between an anomalous example and the points on the data manifold. When training with objective (4) the resulting model, on the one hand, aims to reconstruct the normal regions resulting in a low reconstruction error and on the other hand it amplifies the reconstruction error for the anomalous regions acting almost as a segmentation network. This potentially allows to boost final localization performance - as we showed in the experimental section in Figure 11. In contrast to the pure segmentation approach, however, the resulting model focuses more on the data manifold reducing the overfitting on specific patterns produced by a chosen transformation to create distorted inputs.

Finally, the inference with our method (during training and prediction) is very efficient. Unlike related previous methods, it processes the entire input image in one single step and does not require additional memory space used by approaches based on memory banks of pretrained features. In our experiments on the challenging and publicly available MVTec AD dataset we showed that the new approach achieves state-of-the-art detection and localization performance. On the texture-subset (and some texture-like object categories), in particular, it consistently outperforms a bunch of recent anomaly detection methods for both detection and localization tasks.

REFERENCES

- [1] M. Haselmann, D. P. Gruber, and P. Tabatabai, "Anomaly detection using deep learning based image completion," in *17th IEEE International Conference on Machine Learning and Applications, ICMLA 2018, Orlando, FL, USA, December 17-20, 2018*, M. A. Wani, M. M. Kantardzic, M. S. Mouchaweh, J. Gama, and E. Lughofer, Eds. IEEE, 2018, pp. 1237-1242.
- [2] P. Bergmann, S. Löwe, M. Fauser, D. Sattlegger, and C. Steger, "Improving unsupervised defect segmentation by applying structural similarity to autoencoders," in *Proceedings of the 14th International Joint Conference on Computer Vision, Imaging and Computer Graphics Theory and Applications, VISIGRAPP 2019, Volume 5: VISAPP, Prague, Czech Republic, February 25-27, 2019*, A. Trémeau, G. M. Farinella, and J. Braz, Eds. SciTePress, 2019, pp. 372-380.
- [3] L. Wang, D. Zhang, J. Guo, and Y. Han, "Image anomaly detection using normal data only by latent space resampling," *Applied Sciences*, vol. 10, no. 23, 2020.
- [4] P. Bergmann, M. Fauser, D. Sattlegger, and C. Steger, "Uninformed students: Student-teacher anomaly detection with discriminative latent embeddings," in *2020 IEEE/CVF Conference on Computer Vision and Pattern Recognition, CVPR 2020, Seattle, WA, USA, June 13-19, 2020*. Computer Vision Foundation / IEEE, 2020, pp. 4182-4191.
- [5] S. Venkataramanan, K. Peng, R. V. Singh, and A. Mahalanobis, "Attention guided anomaly localization in images," in *Computer Vision - ECCV 2020 - 16th European Conference, Glasgow, UK, August 23-28, 2020, Proceedings, Part XVII*, ser. Lecture Notes in Computer Science, A. Vedaldi, H. Bischof, T. Brox, and J. Frahm, Eds., vol. 12362. Springer, 2020, pp. 485-503.

- [6] T. Schlegl, P. Seeböck, S. M. Waldstein, U. Schmidt-Erfurth, and G. Langs, "Unsupervised anomaly detection with generative adversarial networks to guide marker discovery," in *Information Processing in Medical Imaging - 25th International Conference, IPMI 2017, Boone, NC, USA, June 25-30, 2017, Proceedings*, ser. Lecture Notes in Computer Science, M. Niethammer, M. Styner, S. R. Aylward, H. Zhu, I. Oguz, P. Yap, and D. Shen, Eds., vol. 10265. Springer, 2017, pp. 146–157.
- [7] P. Napolitano, F. Piccoli, and R. Schettini, "Anomaly detection in nanofibrous materials by cnn-based self-similarity," *Sensors*, vol. 18, no. 1, p. 209, 2018.
- [8] T. Böttger and M. Ulrich, "Real-time texture error detection on textured surfaces with compressed sensing," *Pattern Recognit. Image Anal.*, vol. 26, pp. 88–94, 2016.
- [9] W. Liu, R. Li, M. Zheng, S. Karanam, Z. Wu, B. Bhanu, R. J. Radke, and O. I. Camps, "Towards visually explaining variational autoencoders," in *2020 IEEE/CVF Conference on Computer Vision and Pattern Recognition, CVPR 2020, Seattle, WA, USA, June 13-19, 2020*. IEEE, 2020, pp. 8639–8648.
- [10] K. Roth, L. Pemula, J. Zepeda, B. Schölkopf, T. Brox, and P. V. Gehler, "Towards total recall in industrial anomaly detection," in *IEEE/CVF Conference on Computer Vision and Pattern Recognition, CVPR 2022, New Orleans, LA, USA, June 18-24, 2022*. IEEE, 2022, pp. 14298–14308.
- [11] Q. Wan, L. Gao, X. Li, and L. Wen, "Industrial image anomaly localization based on gaussian clustering of pretrained feature," *IEEE Trans. Ind. Electron.*, vol. 69, no. 6, pp. 6182–6192, 2022.
- [12] X. Chen and E. Konukoglu, "Unsupervised detection of lesions in brain MRI using constrained adversarial autoencoders," *CoRR*, vol. abs/1806.04972, 2018. [Online]. Available: <http://arxiv.org/abs/1806.04972>
- [13] T. Schlegl, P. Seeböck, S. M. Waldstein, G. Langs, and U. Schmidt-Erfurth, "f-anogan: Fast unsupervised anomaly detection with generative adversarial networks," *Medical Image Anal.*, vol. 54, pp. 30–44, 2019.
- [14] J. Tan, B. Hou, T. Day, J. M. Simpson, D. Rueckert, and B. Kainz, "Detecting outliers with poisson image interpolation," in *Medical Image Computing and Computer Assisted Intervention - MICCAI 2021 - 24th International Conference, Strasbourg, France, September 27 - October 1, 2021, Proceedings, Part V*, ser. Lecture Notes in Computer Science, M. de Bruijne, P. C. Cattin, S. Cotin, N. Padoy, S. Speidel, Y. Zheng, and C. Essert, Eds., vol. 12905. Springer, 2021, pp. 581–591.
- [15] D. Zimmerer, F. Isensee, J. Petersen, S. Kohl, and K. H. Maier-Hein, "Unsupervised anomaly localization using variational autoencoders," in *Medical Image Computing and Computer Assisted Intervention - MICCAI 2019 - 22nd International Conference, Shenzhen, China, October 13-17, 2019, Proceedings, Part IV*, ser. Lecture Notes in Computer Science, D. Shen, T. Liu, T. M. Peters, L. H. Staib, C. Essert, S. Zhou, P. Yap, and A. R. Khan, Eds., vol. 11767. Springer, 2019, pp. 289–297.
- [16] D. Abati, A. Porrello, S. Calderara, and R. Cucchiara, "Latent space autoregression for novelty detection," in *IEEE Conference on Computer Vision and Pattern Recognition, CVPR 2019, Long Beach, CA, USA, June 16-20, 2019*. Computer Vision Foundation / IEEE, 2019, pp. 481–490.
- [17] T. Defard, A. Setkov, A. Loesch, and R. Audigier, "Padim: A patch distribution modeling framework for anomaly detection and localization," in *Pattern Recognition. ICPR International Workshops and Challenges - Virtual Event, January 10-15, 2021, Proceedings, Part IV*, ser. Lecture Notes in Computer Science, A. D. Bimbo, R. Cucchiara, S. Sclaroff, G. M. Farinella, T. Mei, M. Bertini, H. J. Escalante, and R. Vezzani, Eds., vol. 12664. Springer, 2020, pp. 475–489.
- [18] B. Schölkopf, J. C. Platt, J. Shawe-Taylor, A. J. Smola, and R. C. Williamson, "Estimating the support of a high-dimensional distribution," *Neural Comput.*, vol. 13, no. 7, pp. 1443–1471, 2001.
- [19] L. Ruff, N. Görnitz, L. Deecke, S. A. Siddiqui, R. A. Vandermeulen, A. Binder, E. Müller, and M. Kloft, "Deep one-class classification," in *Proceedings of the 35th International Conference on Machine Learning, ICML 2018, Stockholmsmässan, Stockholm, Sweden, July 10-15, 2018*, ser. Proceedings of Machine Learning Research, J. G. Dy and A. Krause, Eds., vol. 80. PMLR, 2018, pp. 4390–4399.
- [20] K. H. Kim, S. Shim, Y. Lim, J. Jeon, J. Choi, B. Kim, and A. S. Yoon, "Rapp: Novelty detection with reconstruction along projection pathway," in *8th International Conference on Learning Representations, ICLR 2020, Addis Ababa, Ethiopia, April 26-30, 2020*. OpenReview.net, 2020.
- [21] S. Lee, S. Lee, and B. C. Song, "CFA: coupled-hypersphere-based feature adaptation for target-oriented anomaly localization," *IEEE Access*, vol. 10, pp. 78 446–78 454, 2022.
- [22] D. Kim, C. Park, S. Cho, and S. Lee, "FAPM: fast adaptive patch memory for real-time industrial anomaly detection," *CoRR*, vol. abs/2211.07381, 2022. [Online]. Available: <https://doi.org/10.48550/arXiv.2211.07381>
- [23] J. Bae, J. Lee, and S. Kim, "Image anomaly detection and localization with position and neighborhood information," *CoRR*, vol. abs/2211.12634, 2022. [Online]. Available: <https://doi.org/10.48550/arXiv.2211.12634>
- [24] C. Tsai, T. Wu, and S. Lai, "Multi-scale patch-based representation learning for image anomaly detection and segmentation," in *IEEE/CVF Winter Conference on Applications of Computer Vision, WACV 2022, Waikoloa, HI, USA, January 3-8, 2022*. IEEE, 2022, pp. 3065–3073.
- [25] Y. Zou, J. Jeong, L. Pemula, D. Zhang, and O. Dabeer, "Spot-the-difference self-supervised pre-training for anomaly detection and segmentation," in *Computer Vision - ECCV 2022 - 17th European Conference, Tel Aviv, Israel, October 23-27, 2022, Proceedings, Part XXX*, ser. Lecture Notes in Computer Science, S. Avidan, G. J. Brostow, M. Cissé, G. M. Farinella, and T. Hassner, Eds., vol. 13690. Springer, 2022, pp. 392–408.
- [26] N. Cohen and Y. Hoshen, "Sub-image anomaly detection with deep pyramid correspondences," *CoRR*, vol. abs/2005.02357, 2020. [Online]. Available: <https://arxiv.org/abs/2005.02357>
- [27] N. Li, K. Jiang, Z. Ma, X. Wei, X. Hong, and Y. Gong, "Anomaly detection via self-organizing map," in *2021 IEEE International Conference on Image Processing, ICIP 2021, Anchorage, AK, USA, September 19-22, 2021*. IEEE, 2021, pp. 974–978.
- [28] M. Salehi, N. Sadjadi, S. Baselizadeh, M. H. Rohban, and H. R. Rabiee, "Multiresolution knowledge distillation for anomaly detection," in *IEEE Conference on Computer Vision and Pattern Recognition, CVPR 2021, virtual, June 19-25, 2021*. Computer Vision Foundation / IEEE, 2021, pp. 14 902–14 912.
- [29] H. Deng and X. Li, "Anomaly detection via reverse distillation from one-class embedding," in *IEEE/CVF Conference on Computer Vision and Pattern Recognition, CVPR 2022, New Orleans, LA, USA, June 18-24, 2022*. IEEE, 2022, pp. 9727–9736.
- [30] M. Rudolph, T. Wehrbein, B. Rosenhahn, and B. Wandt, "Asymmetric student-teacher networks for industrial anomaly detection," in *IEEE/CVF Winter Conference on Applications of Computer Vision, WACV 2023, Waikoloa, HI, USA, January 2-7, 2023*. IEEE, 2023, pp. 2591–2601.
- [31] Y. Cao, Q. Wan, W. Shen, and L. Gao, "Informative knowledge distillation for image anomaly segmentation," *Knowl. Based Syst.*, vol. 248, p. 108846, 2022.
- [32] K. Zhang, B. Wang, and C. J. Kuo, "Pedenet: Image anomaly localization via patch embedding and density estimation," *Pattern Recognit. Lett.*, vol. 153, pp. 144–150, 2022.
- [33] Q. Wan, L. Gao, X. Li, and L. Wen, "Unsupervised image anomaly detection and segmentation based on pretrained feature mapping," *IEEE Trans. Ind. Informatics*, vol. 19, no. 3, pp. 2330–2339, 2023.
- [34] Q. Wan, Y. Cao, L. Gao, W. Shen, and X. Li, "Position encoding enhanced feature mapping for image anomaly detection," in *18th IEEE International Conference on Automation Science and Engineering, CASE 2022, Mexico City, Mexico, August 20-24, 2022*. IEEE, 2022, pp. 876–881.
- [35] Y. Zheng, X. Wang, R. Deng, T. Bao, R. Zhao, and L. Wu, "Focus your distribution: Coarse-to-fine non-contrastive learning for anomaly detection and localization," in *IEEE International Conference on Multimedia and Expo, ICME 2022, Taipei, Taiwan, July 18-22, 2022*. IEEE, 2022, pp. 1–6.
- [36] J. Yu, Y. Zheng, X. Wang, W. Li, Y. Wu, R. Zhao, and L. Wu, "Fastflow: Unsupervised anomaly detection and localization via 2d normalizing flows," *CoRR*, vol. abs/2111.07677, 2021. [Online]. Available: <https://arxiv.org/abs/2111.07677>
- [37] D. A. Gudovskiy, S. Ishizaka, and K. Kozuka, "CFLOW-AD: real-time unsupervised anomaly detection with localization via conditional normalizing flows," in *IEEE/CVF Winter Conference on Applications of Computer Vision, WACV 2022, Waikoloa, HI, USA, January 3-8, 2022*. IEEE, 2022, pp. 1819–1828.
- [38] Y. Kim, H. Jang, D. Lee, and H. Choi, "Altub: Alternating training method to update base distribution of normalizing flow for

- anomaly detection," *CoRR*, vol. abs/2210.14913, 2022. [Online]. Available: <https://doi.org/10.48550/arXiv.2210.14913>
- [39] J. Yi and S. Yoon, "Patch SVDD: patch-level SVDD for anomaly detection and segmentation," in *Computer Vision - ACCV 2020 - 15th Asian Conference on Computer Vision, Kyoto, Japan, November 30 - December 4, 2020, Revised Selected Papers, Part VI*, ser. Lecture Notes in Computer Science, H. Ishikawa, C. Liu, T. Pajdla, and J. Shi, Eds., vol. 12627. Springer, 2020, pp. 375–390.
- [40] C. Hu, K. Chen, and H. Shao, "A semantic-enhanced method based on deep SVDD for pixel-wise anomaly detection," in *2021 IEEE International Conference on Multimedia and Expo, ICME 2021, Shenzhen, China, July 5-9, 2021*. IEEE, 2021, pp. 1–6.
- [41] M. Yang, P. Wu, and H. Feng, "Memseg: A semi-supervised method for image surface defect detection using differences and commonalities," *Eng. Appl. Artif. Intell.*, vol. 119, p. 105835, 2023.
- [42] Y. Yan, D. Wang, G. Zhou, and Q. Chen, "Unsupervised anomaly segmentation via multilevel image reconstruction and adaptive attention-level transition," *IEEE Trans. Instrum. Meas.*, vol. 70, pp. 1–12, 2021.
- [43] A. Collin and C. D. Vleeschouwer, "Improved anomaly detection by training an autoencoder with skip connections on images corrupted with stain-shaped noise," in *25th International Conference on Pattern Recognition, ICPR 2020, Virtual Event / Milan, Italy, January 10-15, 2021*. IEEE, 2020, pp. 7915–7922.
- [44] X. Tao, D. Zhang, W. Ma, Z. Hou, Z. Lu, and C. Adak, "Unsupervised anomaly detection for surface defects with dual-siamese network," *IEEE Trans. Ind. Informatics*, vol. 18, no. 11, pp. 7707–7717, 2022.
- [45] T. Liu, B. Li, Z. Zhao, X. Du, B. Jiang, and L. Geng, "Reconstruction from edge image combined with color and gradient difference for industrial surface anomaly detection," *CoRR*, vol. abs/2210.14485, 2022. [Online]. Available: <https://doi.org/10.48550/arXiv.2210.14485>
- [46] D. Kim, D. Jeong, H. Kim, K. Chong, S. Kim, and H. Cho, "Spatial contrastive learning for anomaly detection and localization," *IEEE Access*, vol. 10, pp. 17 366–17 376, 2022.
- [47] C. Huang, Q. Xu, Y. Wang, Y. Wang, and Y. Zhang, "Self-supervised masking for unsupervised anomaly detection and localization," *CoRR*, vol. abs/2205.06568, 2022. [Online]. Available: <https://doi.org/10.48550/arXiv.2205.06568>
- [48] P. Liznerski, L. Ruff, R. A. Vandermeulen, B. J. Franks, M. Kloft, and K. R. Müller, "Explainable deep one-class classification," in *9th International Conference on Learning Representations, ICLR 2021, Virtual Event, Austria, May 3-7, 2021*. OpenReview.net, 2021.
- [49] C. Li, K. Sohn, J. Yoon, and T. Pfister, "Cutpaste: Self-supervised learning for anomaly detection and localization," in *IEEE Conference on Computer Vision and Pattern Recognition, CVPR 2021, virtual, June 19-25, 2021*. Computer Vision Foundation / IEEE, 2021, pp. 9664–9674.
- [50] J. Pirnay and K. Chai, "Inpainting transformer for anomaly detection," in *Image Analysis and Processing - ICIAP 2022 - 21st International Conference, Lecce, Italy, May 23-27, 2022, Proceedings, Part II*, ser. Lecture Notes in Computer Science, S. Sclaroff, C. Distanto, M. Leo, G. M. Farinella, and F. Tombari, Eds., vol. 13232. Springer, 2022, pp. 394–406.
- [51] V. Zavrtnik, M. Kristan, and D. Skocaj, "Dræm - A discriminatively trained reconstruction embedding for surface anomaly detection," in *2021 IEEE/CVF International Conference on Computer Vision, ICCV 2021, Montreal, QC, Canada, October 10-17, 2021*. IEEE, 2021, pp. 8310–8319.
- [52] J. Bae, J.-H. Lee, and S. Kim, "Pni: Industrial anomaly detection using position and neighborhood information," in *arXiv:2211.12634*, 2023.
- [53] H. M. Schlüter, J. Tan, B. Hou, and B. Kainz, "Natural synthetic anomalies for self-supervised anomaly detection and localization," in *Computer Vision - ECCV 2022 - 17th European Conference, Tel Aviv, Israel, October 23-27, 2022, Proceedings, Part XXXI*, ser. Lecture Notes in Computer Science, S. Avidan, G. J. Brostow, M. Cissé, G. M. Farinella, and T. Hassner, Eds., vol. 13691. Springer, 2022, pp. 474–489.
- [54] D. Dehaene, O. Frigo, S. Combexelle, and P. Eline, "Iterative energy-based projection on a normal data manifold for anomaly localization," in *8th International Conference on Learning Representations, ICLR 2020, Addis Ababa, Ethiopia, April 26-30, 2020*. OpenReview.net, 2020.
- [55] J. W. Song, K. Kong, Y. I. Park, S. G. Kim, and S. Kang, "Anoseg: Anomaly segmentation network using self-supervised learning," *CoRR*, vol. abs/2110.03396, 2021. [Online]. Available: <https://arxiv.org/abs/2110.03396>
- [56] Y. Lee and P. Kang, "Anovit: Unsupervised anomaly detection and localization with vision transformer-based encoder-decoder," *IEEE Access*, vol. 10, pp. 46 717–46 724, 2022.
- [57] J. Jiang, J. Zhu, M. Bilal, Y. Cui, N. Kumar, R. Dou, F. Su, and X. Xu, "Masked swin transformer unet for industrial anomaly detection," *IEEE Trans. Ind. Informatics*, vol. 19, no. 2, pp. 2200–2209, 2023.
- [58] J. Wu, D. Chen, C. Fuh, and T. Liu, "Learning unsupervised metaformer for anomaly detection," in *2021 IEEE/CVF International Conference on Computer Vision, ICCV 2021, Montreal, QC, Canada, October 10-17, 2021*. IEEE, 2021, pp. 4349–4358.
- [59] X. Jiang, J. Liu, J. Wang, Q. Nie, K. Wu, Y. Liu, C. Wang, and F. Zheng, "Softpatch: Unsupervised anomaly detection with noisy data," in *NeurIPS*, 2022.
- [60] L. Ruff, J. R. Kauffmann, R. A. Vandermeulen, W. Samek, M. Kloft, T. G. Dietterich, and K. R. Müller, "A unifying review of deep and shallow anomaly detection," *Proc. IEEE*, vol. 109, no. 5, pp. 756–795, 2021.
- [61] D. M. J. Tax and R. P. W. Duin, "Support vector data description," *Mach. Learn.*, vol. 54, no. 1, pp. 45–66, 2004.
- [62] P. Chong, L. Ruff, M. Kloft, and A. Binder, "Simple and effective prevention of mode collapse in deep one-class classification," in *2020 International Joint Conference on Neural Networks, IJCNN 2020, Glasgow, United Kingdom, July 19-24, 2020*. IEEE, 2020, pp. 1–9.
- [63] C. Hu, Y. Feng, H. Kamigaito, H. Takamura, and M. Okumura, "One-class text classification with multi-modal deep support vector data description," in *Proceedings of the 16th Conference of the European Chapter of the Association for Computational Linguistics: Main Volume, EACL 2021, Online, April 19 - 23, 2021*, P. Merlo, J. Tiedemann, and R. Tsarfaty, Eds. Association for Computational Linguistics, 2021, pp. 3378–3390.
- [64] P. Vincent, H. Larochelle, Y. Bengio, and P. Manzagol, "Extracting and composing robust features with denoising autoencoders," in *Machine Learning, Proceedings of the Twenty-Fifth International Conference (ICML 2008), Helsinki, Finland, June 5-9, 2008*, ser. ACM International Conference Proceeding Series, W. W. Cohen, A. McCallum, and S. T. Roweis, Eds., vol. 307. ACM, 2008, pp. 1096–1103.
- [65] J. Deng, Z. Zhang, E. Marchi, and B. W. Schuller, "Sparse autoencoder-based feature transfer learning for speech emotion recognition," in *2013 Humaine Association Conference on Affective Computing and Intelligent Interaction, ACII 2013, Geneva, Switzerland, September 2-5, 2013*. IEEE Computer Society, 2013, pp. 511–516.
- [66] D. Pathak, P. Krähenbühl, J. Donahue, T. Darrell, and A. A. Efros, "Context encoders: Feature learning by inpainting," in *2016 IEEE Conference on Computer Vision and Pattern Recognition, CVPR 2016, Las Vegas, NV, USA, June 27-30, 2016*. IEEE Computer Society, 2016, pp. 2536–2544.
- [67] S. Iizuka, E. Simo-Serra, and H. Ishikawa, "Globally and locally consistent image completion," *ACM Trans. Graph.*, vol. 36, no. 4, pp. 107:1–107:14, 2017.
- [68] J. Yu, Z. Lin, J. Yang, X. Shen, X. Lu, and T. S. Huang, "Generative image inpainting with contextual attention," in *2018 IEEE Conference on Computer Vision and Pattern Recognition, CVPR 2018, Salt Lake City, UT, USA, June 18-22, 2018*. IEEE Computer Society, 2018, pp. 5505–5514.
- [69] G. Liu, F. A. Reda, K. J. Shih, T. Wang, A. Tao, and B. Catanzaro, "Image inpainting for irregular holes using partial convolutions," in *Computer Vision - ECCV 2018 - 15th European Conference, Munich, Germany, September 8-14, 2018, Proceedings, Part XI*, ser. Lecture Notes in Computer Science, V. Ferrari, M. Hebert, C. Sminchisescu, and Y. Weiss, Eds., vol. 11215. Springer, 2018, pp. 89–105.
- [70] J. Yu, Z. Lin, J. Yang, X. Shen, X. Lu, and T. S. Huang, "Free-form image inpainting with gated convolution," in *2019 IEEE/CVF International Conference on Computer Vision, ICCV 2019, Seoul, Korea (South), October 27 - November 2, 2019*. IEEE, 2019, pp. 4470–4479.
- [71] P. Bergmann, M. Fauser, D. Sattlegger, and C. Steger, "Mvtec AD - A comprehensive real-world dataset for unsupervised anomaly detection," in *IEEE Conference on Computer Vision and Pattern Recognition, CVPR 2019, Long Beach, CA, USA, June 16-20, 2019*. Computer Vision Foundation / IEEE, 2019, pp. 9592–9600.
- [72] P. Bergmann, K. Batzner, M. Fauser, D. Sattlegger, and C. Steger, "The mvtec anomaly detection dataset: A comprehensive real-world dataset for unsupervised anomaly detection," *Int. J. Comput. Vis.*, vol. 129, no. 4, pp. 1038–1059, 2021.

- [73] V. Zavrtanik, M. Kristan, and D. Skocaj, "Reconstruction by inpainting for visual anomaly detection," *Pattern Recognit.*, vol. 112, p. 107706, 2021.
- [74] J. Kauffmann, K.-R. Müller, and G. Montavon, "Towards explaining anomalies: A deep Taylor decomposition of one-class models," *Pattern Recognition*, vol. 101, p. 107198, 2020.
- [75] J. Kauffmann, M. Esders, L. Ruff, G. Montavon, W. Samek, and K.-R. Müller, "From clustering to cluster explanations via neural networks," *IEEE Transactions on Neural Networks and Learning Systems*, pp. 1–15, 2022.
- [76] W. Samek, G. Montavon, S. Lapuschkin, C. J. Anders, and K. R. Müller, "Explaining deep neural networks and beyond: A review of methods and applications," *Proc. IEEE*, vol. 109, no. 3, pp. 247–278, 2021.
- [77] R. R. Selvaraju, M. Cogswell, A. Das, R. Vedantam, D. Parikh, and D. Batra, "Grad-cam: Visual explanations from deep networks via gradient-based localization," *Int. J. Comput. Vis.*, vol. 128, no. 2, pp. 336–359, 2020.
- [78] R. Schuster, O. Wasenmüller, C. Unger, and D. Stricker, "SDC - stacked dilated convolution: A unified descriptor network for dense matching tasks," in *IEEE Conference on Computer Vision and Pattern Recognition, CVPR 2019, Long Beach, CA, USA, June 16-20, 2019*. Computer Vision Foundation / IEEE, 2019, pp. 2556–2565.
- [79] D. Koller and N. Friedman, *Probabilistic Graphical Models: Principles and Techniques - Adaptive Computation and Machine Learning*. The MIT Press, 2009.
- [80] M. J. Wainwright and M. I. Jordan, "Graphical models, exponential families, and variational inference," *Foundations and Trends in Machine Learning*, vol. 1, no. 1-2, pp. 1–305, 2008.
- [81] J. Lafferty, "Conditional random fields: Probabilistic models for segmenting and labeling sequence data," in *ICML*. Morgan Kaufmann, 2001, pp. 282–289.
- [82] A. Bauer, S. Nakajima, and K.-R. Müller, "Efficient exact inference with loss augmented objective in structured learning," *IEEE Trans. Neural Netw. Learning Syst.*, vol. 28, no. 11, pp. 2566 – 2579, 2017.
- [83] A. Bauer, S. Nakajima, N. Görnitz, and K.-R. Müller, "Partial optimality of dual decomposition for map inference in pairwise mrfs," in *Proceedings of Machine Learning Research*, ser. Proceedings of Machine Learning Research, K. Chaudhuri and M. Sugiyama, Eds., vol. 89, 16–18 Apr 2019, pp. 1696–1703.
- [84] A. Bauer, S. Nakajima, and K.-R. Müller, "Polynomial-time constrained message passing for exact map inference on discrete models with global dependencies," *Mathematics*, vol. 11, no. 12, 2023. [Online]. Available: <https://www.mdpi.com/2227-7390/11/12/2628>
- [85] D. P. Kingma and J. Ba, "Adam: A method for stochastic optimization," in *3rd International Conference on Learning Representations, ICLR 2015, San Diego, CA, USA, May 7-9, 2015, Conference Track Proceedings*, Y. Bengio and Y. LeCun, Eds., 2015.
- [86] Z. Wang, A. C. Bovik, H. R. Sheikh, and E. P. Simoncelli, "Image quality assessment: from error visibility to structural similarity," *IEEE Trans. Image Process.*, vol. 13, no. 4, pp. 600–612, 2004.

SUPPLEMENTS

1 PROOF OF PROPOSITION 1

In order to prove Proposition 1 we first introduce a few auxiliary lemmas. We also extend the notation as follows. Given a vector $\mathbf{x} \in \mathbb{R}^N$ and a set of indices $S \subset \{1, \dots, N\}$ and its complement $\bar{S} := \{1, \dots, N\} \setminus S$, we interpret the restriction \mathbf{x}_S in two different ways depending on the context either as an element $\mathbf{x}_S \in \mathbb{R}^{|S|}$ or as an element $\mathbf{x}_S \in \mathbb{R}^N$ where the indices in \bar{S} are set to zeros, that is, $\mathbf{x}_{\bar{S}} = \mathbf{0} \in \mathbb{R}^{|\bar{S}|}$. Given such notation, we can write $\mathbf{x} = \mathbf{x}_S + \mathbf{x}_{\bar{S}}$.

Lemma 1. For all $\mathbf{x}, \mathbf{y} \in \mathbb{R}^N$, $N \in \mathbb{N}$ the following statement holds:

$$\mathbf{x}^T \mathbf{y} = 0 \implies \|\mathbf{x}\|^2 + \|\mathbf{y}\|^2 = \|\mathbf{x} - \mathbf{y}\|^2 = \|\mathbf{x} + \mathbf{y}\|^2 \quad (15)$$

Proof:

$$\|\mathbf{x} \pm \mathbf{y}\|^2 = \|\mathbf{x}\|^2 + \|\mathbf{y}\|^2 \pm \underbrace{2\mathbf{x}^T \mathbf{y}}_{=0} = \|\mathbf{x}\|^2 + \|\mathbf{y}\|^2$$

□

Lemma 2. For all $\mathbf{x}, \mathbf{y} \in \mathbb{R}^N$, $N \in \mathbb{N}$ the following statement holds:

$$\exists \lambda > 0: \mathbf{x} = \lambda \cdot \mathbf{y} \implies \left| \|\mathbf{x}\|^2 - \|\mathbf{y}\|^2 \right| \leq \|\mathbf{x} + \mathbf{y}\|^2 \quad (16)$$

Proof:

$$\begin{aligned} \left| \|\mathbf{x}\|^2 - \|\mathbf{y}\|^2 \right| &\leq \|\mathbf{x}\|^2 + \|\mathbf{y}\|^2 \\ &\stackrel{(*)}{\leq} \|\mathbf{x}\|^2 + \|\mathbf{y}\|^2 + 2\mathbf{x}^T \mathbf{y} \\ &= \|\mathbf{x} + \mathbf{y}\|^2 \end{aligned}$$

where the second step (*) we used our assumption $\mathbf{x} = \lambda \cdot \mathbf{y}$, that is, $2\mathbf{x}^T \mathbf{y} = 2\lambda \mathbf{y}^T \mathbf{y} \geq 0$.

□

Lemma 3. For all $\hat{\mathbf{x}}, \mathbf{x}, \mathbf{y} \in \mathbb{R}^N$, $N \in \mathbb{N}$ with $\hat{\mathbf{x}}_{\bar{S}} = \mathbf{x}_{\bar{S}}$ for some non-empty set of indices $S \subset \{1, \dots, N\}$ and its complement $\bar{S} := \{1, \dots, N\} \setminus S$, the following statement holds:

$$\begin{aligned} \|\hat{\mathbf{x}} - \mathbf{x}\| &\leq \|\hat{\mathbf{x}} - \mathbf{y}\| \iff \\ \|\hat{\mathbf{x}}_S - \mathbf{x}_S\|^2 - \|\hat{\mathbf{x}}_S - \mathbf{y}_S\|^2 &\leq \|\mathbf{x}_{\bar{S}} - \mathbf{y}_{\bar{S}}\|^2. \end{aligned} \quad (17)$$

Proof:

$$\begin{aligned} \|\hat{\mathbf{x}} - \mathbf{x}\| &\leq \|\hat{\mathbf{x}} - \mathbf{y}\| \iff \\ \|\hat{\mathbf{x}} - \mathbf{x}\|^2 &\leq \|\hat{\mathbf{x}} - \mathbf{y}\|^2 \iff \\ \|(\hat{\mathbf{x}}_S - \mathbf{x}_S) + (\hat{\mathbf{x}}_{\bar{S}} - \mathbf{x}_{\bar{S}})\|^2 &\leq \|(\hat{\mathbf{x}}_S - \mathbf{y}_S) + (\hat{\mathbf{x}}_{\bar{S}} - \mathbf{y}_{\bar{S}})\|^2 \stackrel{(*)}{\iff} \\ \|\hat{\mathbf{x}}_S - \mathbf{x}_S\|^2 &\leq \|\hat{\mathbf{x}}_S - \mathbf{y}_S\|^2 + \|\hat{\mathbf{x}}_{\bar{S}} - \mathbf{y}_{\bar{S}}\|^2 \iff \\ \|\hat{\mathbf{x}}_S - \mathbf{x}_S\|^2 - \|\hat{\mathbf{x}}_S - \mathbf{y}_S\|^2 &\leq \|\hat{\mathbf{x}}_{\bar{S}} - \mathbf{y}_{\bar{S}}\|^2 \end{aligned}$$

where in step (*) we used our assumption $\hat{\mathbf{x}}_{\bar{S}} = \mathbf{x}_{\bar{S}}$ and Lemma 1.

□

We now prove Proposition 1.

Proof: The condition in (6) can be divided in two (non-disjoint) cases which we will distinguish shortly. It holds:

$$\begin{aligned} &\|\hat{\mathbf{x}}_S - \mathbf{x}_S\|^2 - \|\hat{\mathbf{x}}_S - \mathbf{y}_S\|^2 \\ &= \|(\hat{\mathbf{x}}_S - \tilde{\mathbf{x}}_S) + (\tilde{\mathbf{x}}_S - \mathbf{x}_S)\|^2 - \|(\hat{\mathbf{x}}_S - \tilde{\mathbf{x}}_S) + (\tilde{\mathbf{x}}_S - \mathbf{y}_S)\|^2 \\ &\stackrel{(L1)}{=} \|\hat{\mathbf{x}}_S - \tilde{\mathbf{x}}_S\|^2 + \|\tilde{\mathbf{x}}_S - \mathbf{x}_S\|^2 - \|\hat{\mathbf{x}}_S - \tilde{\mathbf{x}}_S\|^2 - \|\tilde{\mathbf{x}}_S - \mathbf{y}_S\|^2 \\ &= \|\tilde{\mathbf{x}}_S - \mathbf{x}_S\|^2 - \|\tilde{\mathbf{x}}_S - \mathbf{y}_S\|^2 \\ &\stackrel{(*)}{\leq} \|\mathbf{x}_S - \mathbf{y}_S\|^2 \end{aligned}$$

where in step (L1) we used Lemma 1 and in (*) we distinguished the following two cases.

Case 1: $\|\mathbf{x}_S - \mathbf{y}_S\| = \|\mathbf{x}_S - \tilde{\mathbf{x}}_S\| + \|\tilde{\mathbf{x}}_S - \mathbf{y}_S\|$, that is, $\tilde{\mathbf{x}}_S$ is on the line segment between \mathbf{x}_S and \mathbf{y}_S . In that case the vectors $\mathbf{x}_S - \tilde{\mathbf{x}}_S$ and $\tilde{\mathbf{x}}_S - \mathbf{y}_S$ point in the same direction. It follows from Lemma 2:

$$\begin{aligned} \|\tilde{\mathbf{x}}_S - \mathbf{x}_S\|^2 - \|\tilde{\mathbf{x}}_S - \mathbf{y}_S\|^2 &\stackrel{(L2)}{\leq} \|(\mathbf{x}_S - \tilde{\mathbf{x}}_S) + (\tilde{\mathbf{x}}_S - \mathbf{y}_S)\|^2 \\ &= \|\mathbf{x}_S - \mathbf{y}_S\|^2 \end{aligned}$$

Case 2: $\|\tilde{\mathbf{x}}_S - \mathbf{y}_S\| = \|\tilde{\mathbf{x}}_S - \mathbf{x}_S\| + \|\mathbf{x}_S - \mathbf{y}_S\|$, that is, \mathbf{x}_S is on the line segment between $\tilde{\mathbf{x}}_S$ and \mathbf{y}_S . In particular, that implies: $\|\tilde{\mathbf{x}}_S - \mathbf{x}_S\|^2 - \|\tilde{\mathbf{x}}_S - \mathbf{y}_S\|^2 \leq 0$. It follows:

$$\|\tilde{\mathbf{x}}_S - \mathbf{x}_S\|^2 - \|\tilde{\mathbf{x}}_S - \mathbf{y}_S\|^2 \leq 0 \leq \|\mathbf{x}_S - \mathbf{y}_S\|^2$$

Summarizing the two cases we just showed:

$$\|\hat{\mathbf{x}}_S - \mathbf{x}_S\|^2 - \|\hat{\mathbf{x}}_S - \mathbf{y}_S\|^2 \leq \|\mathbf{x}_S - \mathbf{y}_S\|^2.$$

Finally, using Lemma 3 and the premise $(\|\mathbf{x}_S - \mathbf{y}_S\|^2 \leq \|\mathbf{x}_{\bar{S}} - \mathbf{y}_{\bar{S}}\|^2)$ in (5) in Proposition 1 we can prove our statement:

$$\|\hat{\mathbf{x}}_S - \mathbf{x}_S\|^2 - \|\hat{\mathbf{x}}_S - \mathbf{y}_S\|^2 \leq \|\mathbf{x}_{\bar{S}} - \mathbf{y}_{\bar{S}}\|^2 \stackrel{(L3)}{\implies} \|\hat{\mathbf{x}} - \mathbf{x}\| \leq \|\hat{\mathbf{x}} - \mathbf{y}\|.$$

□

2 PROOF OF THEOREM 1

The claim follows directly from Proposition 1 by identifying $F(\hat{\mathbf{x}})$ in Theorem 1 with \mathbf{x} in Proposition 1.

3 PROOF OF PROPOSITION 2

We now prove Proposition 2.

Proof:

$$\begin{aligned} \mathbf{E} [\|\mathbf{x}_S - \mathbf{y}_S\|^2] &= \mathbf{E} \left[\sum_{i \in S} (x_i - y_i)^2 \right] \\ &= \sum_{i \in S} \mathbf{E} [(x_i - y_i)^2] \\ &= \sum_{i \in S} \mathbf{E} [x_i^2] - 2\mathbf{E} [x_i y_i] + \mathbf{E} [y_i^2] \\ &\stackrel{(*)}{=} |S| \cdot 2 (\mathbf{E} [x_i^2] - \mathbf{E} [x_i]^2) \\ &= |S| \cdot 2 \cdot \underbrace{\mathbf{Var}[x_i]}_{=: \sigma} \end{aligned}$$

where in (*) we used our assumption $P(x_i) = P(x_j)$ and the independence $P(x_i, y_i) = P(x_i) \cdot P(y_i)$ of pixels in different images \mathbf{x} and \mathbf{y} . In particular, that implies $\mathbf{E} [x_i y_i] = \mathbf{E} [x_i] \mathbf{E} [y_i] = \mathbf{E} [x_i]^2$ and $\mathbf{E} [y_i^2] = \mathbf{E} [x_i^2]$.

Similarly, we get

$$\mathbf{E} [\|x_{\bar{S}} - y_{\bar{S}}\|^2] = |\bar{S}| \cdot 2 \cdot \sigma.$$

The claim in the Proposition 2 follows directly from the linearity of the mean.

□

4 WEAK LAW OF BIG NUMBERS FOR MARKOV MODELS AND PROOF OF THEOREM 2

In the following we consider Markov random fields (MRFs), which represent a generalization of Markov chains to multi-dimensions. Such models can be visualized as an undirected graph where the nodes are random variables and the edges encode the statistical dependence between the variables. Given a graph with nodes x_1, \dots, x_N , the *Markov property* of a corresponding MRF assumes conditional independence according to $P(x_i|x_1, \dots, \hat{x}_i, \dots, x_N) = P(x_i|N(x_i))$, where $N(x_i) \subset \{x_1, \dots, \hat{x}_i, \dots, x_N\}$ is a local neighborhood around the node x_i containing all variables which are connected to x_i by an edge. The notation $(x_1, \dots, \hat{x}_i, \dots, x_N)$ implies that x_i is omitted.

Since we are dealing with image tensors, we can assume that the variables representing pixels are organized in a 2-dimensional grid, where each node $x_{i,j}$ is connected to its eight neighbors. That is, $N(x_{i,j}) = \{x_{m,n} : i-1 \leq m \leq i+1, j-1 \leq n \leq j+1\} \setminus \{x_{i,j}\}$. Figure 7 in the main body of the paper illustrates an example of an MRF with 5×5 nodes. The blue area marks the local neighborhood (of order 1) of the node $x_{3,3}$. Similarly to Markov chains we can generalize the notion of a higher order of the Markov property by extending the conditional dependency to the variables further away.

In the following, we assume without loss of generality that the order of the Markov property equals 1. The subsequent proofs can be adjusted to deal with higher orders $k \in \mathbb{N}$. The main requirement here is that k is a constant independent of the number of variables N in the MRF. Based on this assumption, we can derive a version of the weak law of big numbers for Markov models. For this purpose, we define a sequence of growing MRFs by adding new nodes following the grid structure. Furthermore, given an MRF $\{x_1, \dots, x_N\}$, we use the notation $|j-i|_G$ to denote the distance between the nodes x_i and x_j given by the number of edges in a shortest path connecting the two nodes. Note that i and j are some arbitrary indices and do not directly reflect the position of the nodes in a corresponding graph. Later we will consider the limit $|j-i|_G \rightarrow \infty$, which in case of a Markov chain has the following interpretation:

$$\lim_{|j-i|_G \rightarrow \infty} P(x_j|x_i) = \lim_{n \rightarrow \infty} P(x_{i+n}|x_i). \quad (18)$$

Furthermore we denote by $T = (t_{i,j})_{i,j \in I}$ a transition matrix with $t_{i,j} = P(x_k = i | x_l = j)$ where $k, l \in \{1, \dots, N\}$, $i, j \in I$, $|I| < \infty$ and $|l-k|_G = 1$. For the purpose of further derivations, we make an assumption on T described by the following condition:

$$\exists r \in \mathbb{N}_+ \text{ and a column } t_{*,j}^r \text{ in } T^r: t_{i,j}^r > 0 \forall i \in I. \quad (19)$$

Lemma 4. Consider a Markov chain $(x_N)_{N \in \mathbb{N}}$ with a state space I , $|I| < \infty$ and transition matrix T satisfying the condition in (19). The following statements are true:

$$(a) P(x_j|x_i) \rightarrow P(x_j) \text{ for } |j-i|_G \rightarrow \infty. \quad (20)$$

$$(b) \mathbf{E}[x_j|x_i] \rightarrow \mathbf{E}[x_j] \text{ for } |j-i|_G \rightarrow \infty, \quad (21)$$

$$(c) \mathbf{Cov}[x_i, x_j] \rightarrow 0 \text{ for } |j-i|_G \rightarrow \infty. \quad (22)$$

Proof: For a proof of the first statement (a) we refer the reader to the standard literature about Markov chains. We now prove the statement (b).

$$\begin{aligned} \lim_{|j-i|_G \rightarrow \infty} \mathbf{E}[x_j|x_i] &= \lim_{|j-i|_G \rightarrow \infty} \sum_{x_j} x_j P(x_j|x_i) \\ &= \sum_{x_j} x_j \lim_{|j-i|_G \rightarrow \infty} P(x_j|x_i) \\ &= \sum_{x_j} x_j P(x_j) \\ &= \mathbf{E}[x_j] \end{aligned}$$

where in the second step we used $|I| < \infty$ and in the third step the claim in (a).

We now prove the statement in (c). It holds:

$$\begin{aligned} \mathbf{E}_{x_i}[x_i] \mathbf{E}_{x_j}[x_j] &= \mathbf{E}_{x_j}[x_j \mathbf{E}_{x_i}[x_i]] \\ &\stackrel{(b)}{=} \mathbf{E}_{x_j}[x_j \lim_{|j-i|_G \rightarrow \infty} \mathbf{E}_{x_i}[x_i|x_j]] \\ &= \lim_{|j-i|_G \rightarrow \infty} \mathbf{E}_{x_j}[\mathbf{E}_{x_i}[x_i x_j|x_j]] \\ &= \lim_{|j-i|_G \rightarrow \infty} \mathbf{E}_{x_i, x_j}[x_i x_j] \end{aligned}$$

That is,

$$\lim_{|j-i|_G \rightarrow \infty} \mathbf{E}_{x_i, x_j}[x_i x_j] = \mathbf{E}_{x_i}[x_i] \mathbf{E}_{x_j}[x_j]. \quad (23)$$

It follows:

$$\begin{aligned} \lim_{|j-i| \rightarrow \infty} \mathbf{Cov}[x_i, x_j] &= \lim_{|j-i| \rightarrow \infty} (\mathbf{E}_{x_i, x_j}[x_i x_j] - \mathbf{E}_{x_i}[x_i] \mathbf{E}_{x_j}[x_j]) \\ &= \lim_{|j-i| \rightarrow \infty} \mathbf{E}_{x_i, x_j}[x_i x_j] - \mathbf{E}_{x_i}[x_i] \mathbf{E}_{x_j}[x_j] \\ &\stackrel{(23)}{=} \mathbf{E}_{x_i}[x_i] \mathbf{E}_{x_j}[x_j] - \mathbf{E}_{x_i}[x_i] \mathbf{E}_{x_j}[x_j] \\ &= 0. \end{aligned}$$

□

In the following we consider MRFs $\{x_1, \dots, x_N\}$ with N nodes organized in a 2-dimensional grid structure of varying sizes $m \times n$ with m rows and n columns. For $S \subset \{1, \dots, m\}$ we use a notation $\mathbf{x}_{S,j} := \{x_{i,j} : i \in S\}$, with $\mathbf{x}_{*,j}$ denoting the set of all variables in the j -th column of an MRF. Furthermore, we define the notion of a transition matrix $T^{\text{col}} = (t_{i,j}^{\text{col}})$ between the columns of the MRFs as follows:

$$t_{i,j}^{\text{col}} := P(\mathbf{x}_{*,j} = (j_1, \dots, j_m) | \mathbf{x}_{*,i} = (i_1, \dots, i_m)) \quad (24)$$

Note that based on the above definition of the column-transition matrix, the corresponding MRF can be seen a Markov chain with the nodes represented by the columns of our 2-dimensional grid. Given this fact, we can derive the following corollary of Lemma 4.

Corollary 1. Consider a sequence of Markov random fields $(\{x_1, \dots, x_N\})_N$ over a state space I , $|I| < \infty$ with a

fixed number of rows $m \in \mathbb{N}_+$ and growing number of columns $n \in \mathbb{N}_+$, $N = n \cdot m$. Furthermore, assume that the column-transition matrix T^{col} satisfies the condition in (19). Then for all $S \subseteq \{1, \dots, m\}$ the following holds true:

$$P(\mathbf{x}_{S,j} | \mathbf{x}_{*,i}) \longrightarrow P(\mathbf{x}_{S,j}) \text{ for } |j-i|_{\mathbb{G}} \longrightarrow \infty. \quad (25)$$

Proof: First of all, the following fact follows directly from Lemma 4, since our MRFs with column-transition matrix T^{col} can be interpreted as Markov chains:

$$P(\mathbf{x}_{*,j} | \mathbf{x}_{*,i}) \longrightarrow P(\mathbf{x}_{*,j}) \text{ for } |j-i|_{\mathbb{G}} \longrightarrow \infty. \quad (26)$$

Below we use the notation $\bar{S} := \{1, \dots, m\} \setminus S$ to denote the complement of S . It holds:

$$\begin{aligned} P(\mathbf{x}_{S,j} | \mathbf{x}_{*,i}) &= \sum_{\mathbf{x}_{\bar{S},j}} P(\mathbf{x}_{S,j}, \mathbf{x}_{\bar{S},j} | \mathbf{x}_{*,i}) \\ &= \sum_{\mathbf{x}_{\bar{S},j}} P(\mathbf{x}_{*,j} | \mathbf{x}_{*,i}) \end{aligned}$$

It follows:

$$\begin{aligned} \lim_{|j-i|_{\mathbb{G}} \rightarrow \infty} P(\mathbf{x}_{S,j} | \mathbf{x}_{*,i}) &= \lim_{|j-i|_{\mathbb{G}} \rightarrow \infty} \sum_{\mathbf{x}_{\bar{S},j}} P(\mathbf{x}_{*,j} | \mathbf{x}_{*,i}) \\ &\stackrel{(*)}{=} \sum_{\mathbf{x}_{\bar{S},j}} \lim_{|j-i|_{\mathbb{G}} \rightarrow \infty} P(\mathbf{x}_{*,j} | \mathbf{x}_{*,i}) \\ &\stackrel{(26)}{=} \sum_{\mathbf{x}_{\bar{S},j}} P(\mathbf{x}_{*,j}) \\ &= P(\mathbf{x}_{S,j}), \end{aligned}$$

where in step (*) we used $m < \infty$ and $|I| < \infty$.

□

Corollary 2. Consider the setup in Corollary 1. Then the following statements are true:

$$(a) P(x_j | x_i) \longrightarrow P(x_j) \text{ for } |j-i|_{\mathbb{G}} \longrightarrow \infty. \quad (27)$$

$$(b) \mathbf{E}[x_j | x_i] \longrightarrow \mathbf{E}[x_j] \text{ for } |j-i|_{\mathbb{G}} \longrightarrow \infty, \quad (28)$$

$$(c) \mathbf{Cov}[x_i, x_j] \longrightarrow 0 \text{ for } |j-i|_{\mathbb{G}} \longrightarrow \infty. \quad (29)$$

Proof: Here we only prove the claim in (a). Claims (b) and (c) follow directly from (a). See a corresponding proof for Lemma 4 for more details. Remember that our MRFs are 2-dimensional grids with a fixed number of rows m and growing number of columns n . Furthermore, the position of each variable is determined by the row and column index (for example $x_{k,j}$). The running index notation $(x_{1,i}, \dots, \hat{x}_{l,i}, \dots, x_{m,i})$ we use below implies that we sum over all variables $x_{1,i}, \dots, x_{m,i}$ except $x_{l,i}$ for $1 \leq l \leq m$. Note that the following equality holds true

$$\lim_{|j-i|_{\mathbb{G}} \rightarrow \infty} P(x_{k,j}, x_{*,i}) = \lim_{|j-i|_{\mathbb{G}} \rightarrow \infty} P(x_{k,j}) \cdot P(x_{*,i}) \quad (30)$$

since $x_{k,j}$ and $x_{*,i}$ become independent in the limit according to (25).

It follows:

$$\begin{aligned} &\lim_{|j-i| \rightarrow \infty} P(x_{k,j} | x_{l,i}) \\ &= \lim_{|j-i| \rightarrow \infty} \frac{P(x_{k,j}, x_{l,i})}{P(x_{l,i})} \\ &= \lim_{|j-i| \rightarrow \infty} \sum_{(x_{1,i}, \dots, \hat{x}_{l,i}, \dots, x_{m,i})} \frac{P(x_{k,j}, x_{*,i})}{P(x_{l,i})} \\ &\stackrel{(*)}{=} \frac{1}{P(x_{l,i})} \sum_{(x_{1,i}, \dots, \hat{x}_{l,i}, \dots, x_{m,i})} \lim_{|j-i| \rightarrow \infty} P(x_{k,j}, x_{*,i}) \\ &\stackrel{(30)}{=} \frac{1}{P(x_{l,i})} \sum_{(x_{1,i}, \dots, \hat{x}_{l,i}, \dots, x_{m,i})} \lim_{|j-i| \rightarrow \infty} P(x_{k,j}) \cdot P(x_{*,i}) \\ &\stackrel{(*)}{=} \lim_{|j-i| \rightarrow \infty} \frac{P(x_{k,j})}{P(x_{l,i})} \underbrace{\sum_{(x_{1,i}, \dots, \hat{x}_{l,i}, \dots, x_{m,i})} P(x_{*,i})}_{= x_{l,i}} \\ &= P(x_{k,j}), \end{aligned}$$

where in step (*) we used $m < \infty$, $|I| < \infty$ and the fact that all the limits exist.

Note that at the beginning we assumed that the number of rows m in the corresponding MRFs is fixed while the number of columns n is growing. In that case the expression $|i-j|_{\mathbb{G}} \longrightarrow \infty$ has the meaning according to equation (18). However, we can apply the same arguments to the case where the number of columns in an MRF is fixed and the number of rows varies. Finally, we can generalize the above proof to a sequence of MRFs growing in both directions simultaneously justifying the claims (a), (b), (c) with respect to $|i-j|_{\mathbb{G}} \longrightarrow \infty$.

□

After the necessary preparations we now formulate a version of the law of big numbers for Markov models.

Theorem 3. Let $(\{x_1, \dots, x_N\})_{N \in \mathbb{N}}$ be a sequence of Markov random fields over identically distributed variables x_i with $\mathbf{Var}[x_i] < \infty$ and vanishing covariance

$$\mathbf{Cov}[x_i, x_j] \longrightarrow 0 \text{ for } |i-j|_{\mathbb{G}} \longrightarrow \infty. \quad (31)$$

Then the following is true:

$$\frac{1}{N} \sum_{i=1}^N x_i \xrightarrow{P} \mathbf{E}[x_1] \text{ for } N \longrightarrow \infty. \quad (32)$$

Proof: First we reorganize the individual terms by using the variance definition as follows:

$$\begin{aligned} \mathbf{Var} \left[\sum_{i=1}^N x_i \right] &= \mathbf{E} \left[\left(\sum_{i=1}^N x_i - \mathbf{E} \left[\sum_{i=1}^N x_i \right] \right)^2 \right] \\ &= \mathbf{E} \left[\left(\sum_{i=1}^N (x_i - \mathbf{E}[x_i]) \right)^2 \right] \\ &= \sum_{i=1}^N \sum_{j=1}^N \mathbf{Cov}[x_i, x_j] \\ &= \sum_{i=1}^N \mathbf{Var}[x_i] + 2 \sum_{i=1}^N \sum_{j=i+1}^N \mathbf{Cov}[x_i, x_j]. \end{aligned}$$

Let $\epsilon > 0$. Since $\mathbf{Cov}[x_i, x_j]$ converges to zero, there is an $L \in \mathbb{N}$ such that for all i, j satisfying $|i - j|_{\mathbb{G}} > L$ we get $|\mathbf{Cov}[x_i, x_j]| < \epsilon$. Later we will consider $N \rightarrow \infty$. Therefore, we can assume $N > L$ and split the inner sum of the covariance term in the last equation in two sums as follows. Here, we abbreviate the index set $\{j \in \mathbb{N}: i + 1 \leq j \leq N, |i - j|_{\mathbb{G}} \leq L\}$ and $\{j \in \mathbb{N}: i + 1 \leq j \leq N, |i - j|_{\mathbb{G}} > L\}$ by $|i - j|_{\mathbb{G}} \leq L$ and $|i - j|_{\mathbb{G}} > L$, respectively. That is,

$$\begin{aligned} & \sum_{i=1}^N \sum_{j=i+1}^N \mathbf{Cov}[x_i, x_j] \\ &= \sum_{i=1}^N \left(\sum_{j: |i-j|_{\mathbb{G}} \leq L} \underbrace{\mathbf{Cov}[x_i, x_j]}_{\leq \sigma} + \sum_{j: |i-j|_{\mathbb{G}} > L} \underbrace{\mathbf{Cov}[x_i, x_j]}_{< \epsilon} \right) \\ &< N \cdot \frac{L^2}{2} \cdot \sigma + N^2 \cdot \epsilon, \end{aligned}$$

where in the last step we used, on the one hand, the Cauchy-Schwarz inequality $|\mathbf{Cov}[x_i, x_j]| \leq \sqrt{\mathbf{Var}[x_i] \cdot \mathbf{Var}[x_j]} = \mathbf{Var}[x_i] =: \sigma$, and on the other hand, an upper bound on the cardinality of the running index sets given by $\frac{1}{2}L^2$. Altogether, we get the following estimation:

$$\frac{1}{N^2} \mathbf{Var} \left[\sum_{i=1}^N x_i \right] < \frac{\sigma}{N} + \frac{L^2 \cdot \sigma}{N} + \epsilon.$$

Since the first two terms on the right hand side converge to zero (for $N \rightarrow \infty$) and ϵ is chosen arbitrarily small, this implies:

$$\lim_{N \rightarrow \infty} \frac{1}{N^2} \mathbf{Var} \left[\sum_{i=1}^N x_i \right] = 0. \quad (33)$$

Finally, for all $\epsilon > 0$:

$$\begin{aligned} P \left(\left| \frac{1}{N} \sum_{i=1}^N x_i - \mathbf{E}[x_1] \right| > \epsilon \right) &\stackrel{(*)}{\leq} \frac{1}{\epsilon^2} \mathbf{Var} \left[\frac{1}{N} \sum_{i=1}^N x_i \right] \\ &= \frac{1}{\epsilon^2 N^2} \mathbf{Var} \left[\sum_{i=1}^N x_i \right] \end{aligned}$$

where in step (*) we used the Chebyshev's inequality. The convergence

$$\lim_{N \rightarrow \infty} P \left(\left| \frac{1}{N} \sum_{i=1}^N x_i - \mathbf{E}[x_1] \right| > \epsilon \right) = 0 \quad (34)$$

follows from equation (33).

□

Applying Theorem 3 directly to our discussion in the main body of the paper we get the following corollary.

Corollary 3. Consider a pair of sequences of Markov random fields $(\{x_1, \dots, x_N\})_{N \in \mathbb{N}}$, $(\{y_1, \dots, y_N\})_{N \in \mathbb{N}}$ over identically distributed variables x_i, y_j with $\mathbf{Var}[x_i] = \sigma < \infty$ and vanishing covariance

$$\mathbf{Cov}[x_i, x_j] \rightarrow 0 \text{ for } |i - j|_{\mathbb{G}} \rightarrow \infty. \quad (35)$$

Then the following is true:

$$\frac{1}{|S|} \|\mathbf{x}_S - \mathbf{y}_S\|^2 \xrightarrow{P} 2\sigma \text{ for } |S| \rightarrow \infty, \quad (36)$$

where $S \subseteq \{1, \dots, N\}$ denotes a subset of the variable indices.

Based on the above derivations, we now provide a proof for Theorem 2 below.

Proof: Let us assume:

$$\|\mathbf{x}_{\bar{S}} - \mathbf{y}_{\bar{S}}\| < \|\mathbf{x}_S - \mathbf{y}_S\| \leq \sqrt{|S|}, \quad (37)$$

where the last inequality holds due to $x_i, y_j \in [0, 1]$. This implies:

$$\{(\mathbf{x}, \mathbf{y}) : \|\mathbf{x}_{\bar{S}} - \mathbf{y}_{\bar{S}}\| < \|\mathbf{x}_S - \mathbf{y}_S\|\} \subseteq \{(\mathbf{x}, \mathbf{y}) : \|\mathbf{x}_{\bar{S}} - \mathbf{y}_{\bar{S}}\|^2 < |S|\} \quad (38)$$

Consider now the following derivation:

$$\begin{aligned} & \|\mathbf{x}_{\bar{S}} - \mathbf{y}_{\bar{S}}\|^2 < |S| \\ &\iff \frac{1}{|S|} \|\mathbf{x}_{\bar{S}} - \mathbf{y}_{\bar{S}}\|^2 < \frac{|S|}{|S|} \\ &\implies \frac{1}{|S|} \|\mathbf{x}_{\bar{S}} - \mathbf{y}_{\bar{S}}\|^2 < 2\sigma \\ &\implies \left| \frac{1}{|S|} \|\mathbf{x}_{\bar{S}} - \mathbf{y}_{\bar{S}}\|^2 - 2\sigma \right| > 0, \end{aligned}$$

where in the second step we used $|S| \leq 2\sigma|\bar{S}|$. Therefore, it follows from (38):

$$\begin{aligned} & \{(\mathbf{x}, \mathbf{y}) : \|\mathbf{x}_{\bar{S}} - \mathbf{y}_{\bar{S}}\| < \|\mathbf{x}_S - \mathbf{y}_S\|\} \\ &\subseteq \{(\mathbf{x}, \mathbf{y}) : \left| \frac{1}{|S|} \|\mathbf{x}_{\bar{S}} - \mathbf{y}_{\bar{S}}\|^2 - 2\sigma \right| > 0\} \\ &= \{(\mathbf{x}, \mathbf{y}) : \left| \frac{1}{|S|} \|\mathbf{x}_{\bar{S}} - \mathbf{y}_{\bar{S}}\|^2 - 2\sigma \right| > 1\} \cup \\ &\quad \bigcup_{n \geq 2} \{(\mathbf{x}, \mathbf{y}) : \frac{1}{n-1} \geq \left| \frac{1}{|S|} \|\mathbf{x}_{\bar{S}} - \mathbf{y}_{\bar{S}}\|^2 - 2\sigma \right| > \frac{1}{n}\} \end{aligned}$$

Using the above derivations we now upper bound the probability of the corresponding events:

$$\begin{aligned} & P(\|\mathbf{x}_{\bar{S}} - \mathbf{y}_{\bar{S}}\| < \|\mathbf{x}_S - \mathbf{y}_S\|) \\ &\leq P \left(\bigcup_n \left\{ \frac{1}{n-1} \geq \left| \frac{1}{|S|} \|\mathbf{x}_{\bar{S}} - \mathbf{y}_{\bar{S}}\|^2 - 2\sigma \right| > \frac{1}{n} \right\} \right) \\ &\stackrel{(*)}{=} \sum_n P \left(\frac{1}{n-1} \geq \left| \frac{1}{|S|} \|\mathbf{x}_{\bar{S}} - \mathbf{y}_{\bar{S}}\|^2 - 2\sigma \right| > \frac{1}{n} \right), \end{aligned}$$

where in step (*) we used the fact that all the sets in the union are disjoint. Note that we use a short notation \bigcup_n and \sum_n which runs over all previously defined terms (including $n = 1$). Next we consider the above derivations in the limit $N \rightarrow \infty$ for $S \subseteq \{1, \dots, N\}$, $\bar{S} = \{1, \dots, N\} \setminus S$ with a fixed ratio $|S|/|\bar{S}| \leq 2\sigma$. It holds:

$$\begin{aligned} & \lim_{N \rightarrow \infty} P(\|\mathbf{x}_{\bar{S}} - \mathbf{y}_{\bar{S}}\| < \|\mathbf{x}_S - \mathbf{y}_S\|) \\ &\leq \lim_{N \rightarrow \infty} \underbrace{\sum_n P \left(\frac{1}{n-1} \geq \left| \frac{1}{|S|} \|\mathbf{x}_{\bar{S}} - \mathbf{y}_{\bar{S}}\|^2 - 2\sigma \right| > \frac{1}{n} \right)}_{\leq 1} \\ &\stackrel{(*)}{=} \sum_n \lim_{N \rightarrow \infty} P \left(\frac{1}{n-1} \geq \left| \frac{1}{|S|} \|\mathbf{x}_{\bar{S}} - \mathbf{y}_{\bar{S}}\|^2 - 2\sigma \right| > \frac{1}{n} \right) \\ &\leq \sum_n \underbrace{\lim_{N \rightarrow \infty} P \left(\left| \frac{1}{|S|} \|\mathbf{x}_{\bar{S}} - \mathbf{y}_{\bar{S}}\|^2 - 2\sigma \right| > \frac{1}{n} \right)}_{=0} \\ &= 0, \end{aligned}$$

where in step (*) we can swap the limit and the sum signs because the series converges for all $N \in \mathbb{N}$. The last step follows from Corollary 3.

□

As a final remark we note that the assumption in (10) in Theorem 2 automatically holds for any sequence of MRFs, for which the column-transition matrix T^{col} satisfies the condition in (19). The latter does not seem to be a great restriction on the diversity of feasible patterns in the context of real images - as it basically requires that there exists an image $\mathbf{x} \in D$ with a column $\mathbf{x}_{*,i}$ such that the probability of transitioning from this column to any other state $\mathbf{x}_{*,j}$ is bigger than zero, that is, $P(\mathbf{x}_{*,j}|\mathbf{x}_{*,i}) > 0$ for all $\mathbf{x}_{*,j}$. Note that the real images, even those with periodic patterns are subject to random effects like varying lightening condition, dirt particles, or other type of random effects, such that the above requirement with respect to the transition matrix T^{col} is likely to be satisfied for many practical cases.